



THE EVOLUTION OF METALLICITY AND METALLICITY GRADIENTS FROM $z = 2.7$ TO 0.6 WITH KMOS^{3D}

EVA WUYTS¹, EMILY WISNIOSKI¹, MATTEO FOSSATI^{1,2}, NATASCHA M. FÖRSTER SCHREIBER¹, REINHARD GENZEL^{1,3,4}, RIC DAVIES¹, J. TREVOR MENDEL¹, THORSTEN NAAB⁵, BERNHARD RÖTTGERS⁵, DAVID J. WILMAN^{1,2}, STIJN WUYTS⁶, KAUSHALA BANDARA¹, ALESSANDRA BEIFIORI^{1,2}, SIRIO BELLI¹, RALF BENDER^{1,2}, GABRIEL B. BRAMMER⁶, ANDREAS BURKERT⁵, JEFFREY CHAN^{1,2}, AUDREY GALAMETZ¹, SANDESH K. KULKARNI¹, PHILIPP LANG¹, DIETER LUTZ¹, IVELINA G. MOMCHEVA⁷, ERICA J. NELSON⁸, DAVID ROSARIO¹, ROBERTO P. SAGLIA^{1,2}, STELLA SEITZ², LINDA J. TACCONI¹, KEN-ICHI TADAKI¹, HANNAH ÜBLER¹, AND PIETER VAN DOKKUM^{8,9}

¹ Max-Planck-Institut für extraterrestrische Physik, Giessenbachstr. 1, D-85741 Garching, Germany; evawuyts@mpe.mpg.de

² Universitäts-Sternwarte München, Scheinerstr. 1, München, D-81679, Germany

³ Department of Physics, Le Conte Hall, University of California, Berkeley, CA 94720, USA

⁴ Department of Astronomy, Hearst Field Annex, University of California, Berkeley, CA 94720, USA

⁵ Max-Planck Institute for Astrophysics, Karl Schwarzschildstr. 1, D-85748 Garching, Germany

⁶ Department of Physics, University of Bath, Claverton Down, Bath, BA2 7AY, UK

⁷ Space Telescope Science Institute, Baltimore, MD 21218, USA

⁸ Department of Astronomy, Yale University, P.O. Box 208101, New Haven, CT 06520-810, USA

Received 2016 March 1; revised 2016 May 15; accepted 2016 June 4; published 2016 August 9

ABSTRACT

We present measurements of the $[\text{N II}]/\text{H}\alpha$ ratio as a probe of gas-phase oxygen abundance for a sample of 419 star-forming galaxies at $z = 0.6\text{--}2.7$ from the KMOS^{3D} near-IR multi-integral field unit (IFU) survey. The mass–metallicity relation (MZR) is determined consistently with the same sample selection, metallicity tracer, and methodology over the wide redshift range probed by the survey. We find good agreement with long-slit surveys in the literature, except for the low-mass slope of the relation at $z \sim 2.3$, where this sample is less biased than previous samples based on optical spectroscopic redshifts. In this regime we measure a steeper slope than some literature results. Excluding the contribution from active galactic nuclei from the MZR reduces sensitivity at the high-mass end, but produces otherwise consistent results. There is no significant dependence of the $[\text{N II}]/\text{H}\alpha$ ratio on star formation rate at fixed redshift and stellar mass. The IFU data allow spatially resolved measurements of $[\text{N II}]/\text{H}\alpha$, from which we can infer abundance gradients for 180 galaxies, thus tripling the current sample in the literature. The observed gradients are on average flat, with only 15 gradients statistically offset from zero at $>3\sigma$. We have modeled the effect of beam smearing, assuming a smooth intrinsic radial gradient and known seeing, inclination, and effective radius for each galaxy. Our seeing-limited observations can recover up to 70% of the intrinsic gradient for the largest, face-on disks, but only 30% for the smaller, more inclined galaxies. We do not find significant trends between observed or corrected gradients and any stellar population, dynamical, or structural galaxy parameters, mostly in agreement with existing studies with much smaller sample sizes. In cosmological simulations, strong feedback is generally required to produce flat gradients at high redshift.

Key words: galaxies: abundances – galaxies: evolution – galaxies: high-redshift

1. INTRODUCTION

The evolution of the cosmic star formation density and the mass growth of galaxies is largely driven by their available gas reservoirs, as determined from the interplay between gas accretion through cosmic inflow and mergers, star formation, and gas outflows driven by feedback from active galactic nuclei (AGN) and stars (e.g., Genel et al. 2008; Dekel et al. 2009; Bouché et al. 2010; Davé et al. 2012; Lilly et al. 2013; Tacconi et al. 2013). The same processes also determine the metal content of galaxies, its spatial distribution, and its evolution over cosmic time. Observationally, we find a tight correlation between stellar mass and gas-phase oxygen abundance in the local universe, as robustly quantified in the Sloan Digital Sky Survey (SDSS; Tremonti et al. 2004). Theoretical models

explain this relation through a combination of momentum- or energy-driven winds to remove metal-rich gas from the galaxy, inflows of metal-poor gas from the surrounding intergalactic medium, and variations in the star formation efficiency of galaxies (e.g., Dalcanton et al. 2004; Brooks et al. 2007; Finlator & Davé 2008; Spitoni et al. 2010; Peeples & Shankar 2011; Lu et al. 2015). Observational constraints on the mass–metallicity relation (MZR) and its evolution over cosmic time thus provide useful benchmarks for semianalytic and numerical galaxy evolution models addressing the relative importance of gas inflow, enrichment, recycling, and outflow.

Toward higher redshift, an overall decrease in metallicity at fixed stellar mass has been well established with large samples since the recent developments of multi-object spectrographs and the availability of grism data from the *Hubble Space Telescope* (*HST*; e.g., Erb et al. 2006; Zahid et al. 2011; Henry et al. 2013; Stott et al. 2013; Cullen et al. 2014; Steidel et al. 2014; Wuyts et al. 2014; Zahid et al. 2014; Sanders et al. 2015). In absolute terms, the normalization of the MZR evolution remains uncertain due to its dependence on the metallicity indicator used (Kewley & Ellison 2008). Since the

⁹ Based on observations obtained at the Very Large Telescope (VLT) of the European Southern Observatory (ESO), Paranal, Chile (ESO program IDs 092.A-0091, 093.A-0079, 094.A-0217, and 095.A-0047). This work is further based on observations taken by the 3D-*HST* Treasury Program (GO 12177 and 12328) with the NASA/ESA *Hubble Space Telescope*, which is operated by the Association of Universities for Research in Astronomy, Inc., under NASA contract NAS5-26555.

set of observable rest-frame optical emission lines shifts with redshift, studies targeting different redshift ranges typically use different strong-line indicators, which complicates a direct comparison. Additionally, it remains unclear whether for the same indicator the locally derived calibration remains valid at higher redshift given the different photoionization conditions of high- z galaxies (e.g., Kewley et al. 2013; Steidel et al. 2014; Shapley et al. 2015). New approaches using Bayesian analysis or χ^2 minimization for a larger set of emission lines to jointly solve for the galaxy metallicity, as well as interstellar medium (ISM) properties such as ionization parameter and electron density, are attempting to address this (Pérez-Montero 2014; Blanc et al. 2015).

In addition to the total metal content of galaxies, the spatial distribution of heavy elements within galaxies further constrains their baryonic and chemical assembly history. In the local universe, abundance measurements of individual H II regions generally find that galaxies have negative gradients, where the inner regions have higher metallicities than the outer disk regions, indicative of an inside-out growth scenario (Zaritsky et al. 1994; van Zee et al. 1998; Sánchez et al. 2014). There are indications of a flattening of the gradient outside the isophotal radius, possibly due to lower star formation efficiency in the outer disk (e.g., Goddard et al. 2011; Bresolin et al. 2012). Mergers have been found to exhibit flat gradients, likely due to interaction-induced inflow of metal-poor gas in the center and metal mixing (Kewley et al. 2010; Rupke et al. 2010a, 2010b; Perez et al. 2011; Sánchez et al. 2014). At high redshift, dilution from gas infall into the galaxy center has been invoked to explain some observations of positive abundance gradients (Cresci et al. 2010).

The time evolution of abundance gradients can be predicted from classical analytical models of the chemical evolution of the Milky Way disk (Chiappini et al. 2001; Mollá & Díaz 2005; Fu et al. 2009), or from cosmological hydrodynamical simulations (Kobayashi & Nakasato 2011; Rahimi et al. 2011; Few et al. 2012; Pilkington et al. 2012; Gibson et al. 2013; Anglés-Alcázar et al. 2014). Pilkington et al. (2012) find little agreement in an extensive comparison of different simulations and chemical evolution models, which they trace back to the varying treatment of star formation and feedback in the simulations. The impact of the assumed feedback scenario is examined further by Gibson et al. (2013). In this study, “normal” feedback (using 10%–40% of supernova energy to heat the surrounding ISM) predicts steep gradients of $-0.3 \text{ dex kpc}^{-1}$ at $z \sim 2$ that flatten over time, while “enhanced” feedback (including radiation pressure from massive stars) can better redistribute metal-enriched gas over large spatial scales and produces relatively flat gradients at all times. These studies highlight how robust gradient measurements at high redshift can provide powerful constraints on the uncertain nature of stellar feedback processes.

Unfortunately, also the observational measurements present challenges, requiring significant time investments to spatially resolve the fainter emission lines (typically [N II] and/or H β) used in the strong-line metallicity calibrations. The current sample available in the literature consists of 90 gradients at $z = 0.8$ –3.8. Adaptive optics (AO) assisted SINFONI observations have resulted in measured gradients for nine H α -selected HiZELS galaxies at $z = 0.8$ –2.24 (Swinbank et al. 2012) and 19 SINS/zCSINF galaxies at $z = 1.4$ –2.4 (N. M. Förster Schreiber et al. 2016, in preparation). Without AO, there are 26

gradients at $z \sim 1.2$ from MASSIV (Queyrel et al. 2012) and 10 gradients at $z \sim 3$ –4 from AMAZE (Troncoso et al. 2014). Taking advantage of the multiplexing capabilities of KMOS at the VLT, Stott et al. (2014) present a first sample of 20 gradients at $z \sim 0.8$ from HiZELS. There are concerns whether the coarse spatial resolution of seeing-limited observations, typically 5 kpc at $z \sim 2$, can recover the intrinsic gradient (Yuan et al. 2013a). AO-assisted or space-based observations of lensed galaxies can reach spatial resolutions down to 200–300 pc in the source plane. For 16 lensed galaxies with OSIRIS+AO data (Jones et al. 2010, 2013; Yuan et al. 2011; Leethochawalit et al. 2015) and one arc with *HST* grism data from the Grism Lens-Amplified Survey from Space (GLASS; Jones et al. 2015), some steeper gradients have been recovered, but most measurements are comparable to nonlensed samples at similar redshift.

In this work, we exploit the large redshift coverage of the KMOS^{3D} survey from $z = 2.7$ to 0.6 for a consistent study of the evolution of the MZR over 5 billion yr around the period of peak star formation activity in the universe. We use the spatially resolved information unique to our integral field spectroscopic survey to measure abundance gradients for 180 galaxies, thus tripling the total sample. The paper is organized as follows. Section 2 summarizes the KMOS^{3D} sample selection, observations, and data reduction. The MZR and its dependence on the presence of an AGN and on star formation rate (SFR) is analyzed in Section 3. In Section 4 we present the radial abundance gradients and address the effect of beam smearing. Section 5 provides a summary. Throughout this work, we adopt the Chabrier (2003) initial mass function and a flat cosmology with $\Omega_M = 0.3$ and $H_0 = 70 \text{ km s}^{-1} \text{ Mpc}^{-1}$.

2. THE KMOS^{3D} SAMPLE

The galaxies analyzed here are taken from the first 2 yr of the KMOS^{3D} survey, which covers observations up to 2015 April. The survey is described in detail by Wisnioski et al. (2015). KMOS^{3D} is a 5 yr GTO survey with the multi-object near-IR integral field spectrograph KMOS at the VLT (Sharples et al. 2013), which aims to observe a mass-selected sample of >600 galaxies at $z = 0.7$ –2.7 in H α emission to study their spatially resolved kinematics and star formation. Targets are pre-selected to avoid OH skyline contamination based on a combination of existing spectroscopic campaigns and 3D-*HST* grism redshifts from the v4 catalogs (Brammer et al. 2012; Momcheva et al. 2015) in the southern CANDELS fields UDS, COSMOS, and GOODS-S (Grogin et al. 2011; Koekemoer et al. 2011). The availability of near-IR grism data avoids the bias toward bluer colors intrinsic in any selection based only on optical spectroscopic redshifts. Stellar masses, UV+IR SFRs, and global extinction values for the sample are derived from the CANDELS photometry (Skelton et al. 2014) and available far-IR photometry (Lutz et al. 2011; Magnelli et al. 2013), using standard spectral energy distribution (SED) modeling with FAST (Kriek et al. 2009) for a grid of Bruzual & Charlot (2003) models with exponentially declining star formation histories, Calzetti et al. (2000) dust extinction, and solar metallicity (see Wuyts et al. 2011, for details). SFRs are estimated using the ladder of indicators presented by Wuyts et al. (2011) and rely on rest-UV + *Herschel* far-IR or *Spitzer* mid-IR wherever galaxies are individually detected at IR wavelengths, otherwise on the SED-derived SFRs. Morphological parameters such as inclination and effective radius

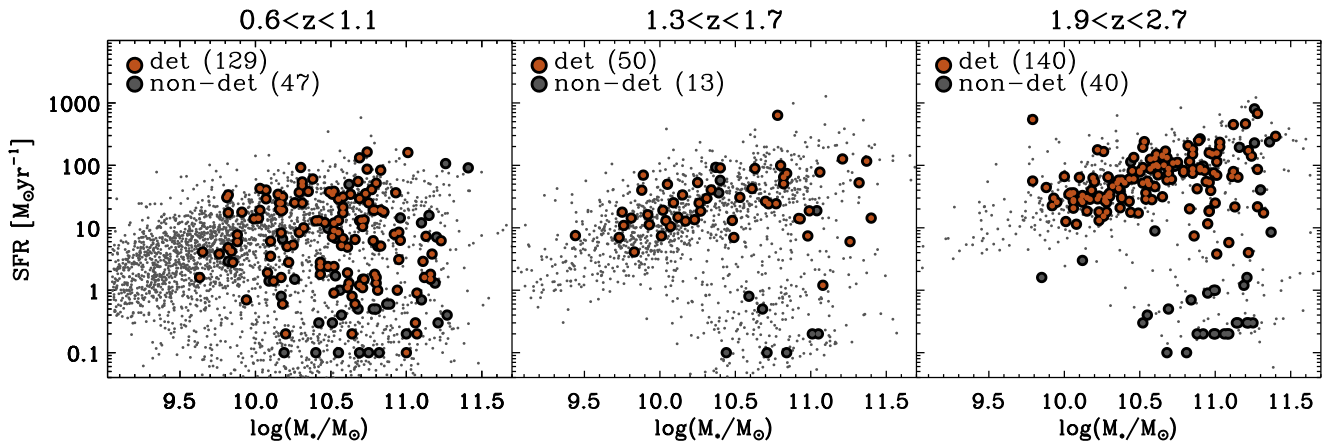


Figure 1. Location of the observed KMOS^{3D} sample in the SED-derived SFR vs. stellar mass plane in three redshift bins. The underlying gray dots represent the full mass-selected galaxy population at $z = 0.6\text{--}2.7$ in the CANDELS fields. Our deep observations probe significantly below the main sequence of star formation.

are available from GALFIT fitting of the F160W CANDELS data by van der Wel et al. (2012).

This work includes 419 targets, 176–63–180 each in the YJ , H and K bands, respectively. The survey strategy deliberately focused on the $z \sim 0.9$ and $z \sim 2.3$ redshift slices first, only now starting to fill in the intermediate range at $z \sim 1.5$ in H band. Figure 1 situates the sample in the star formation versus stellar mass plane. Our deep integrations (baseline of 4–6–8 hr in YJ , H , and K , respectively) allow us to probe significantly below the main sequence of star formation, though in this parameter space the detection fraction drops below our average of 76%, especially in K band.

The data were reduced with the Software Package for Astronomical Reduction with KMOS (SPARK; Davies et al. 2013), complemented with custom IDL scripts for additional flat-fielding, accurate centering, and combining of data taken over multiple epochs, and point-spread function (PSF) characterization. Maps of the $H\alpha$ flux and kinematics are derived with the IDL emission-line fitting code LINEFIT, which was originally developed for SINFONI data (Förster Schreiber et al. 2009; Davies et al. 2011). We mask out all spatial pixels where the signal-to-noise ratio (S/N) in $H\alpha$ drops below 5, as well as outliers in velocity or velocity width or in their respective uncertainties. More details on the data reduction and kinematic mapping can be found in Wisnioski et al. (2015).

Guided by the KMOS^{3D} survey design, which targets primarily $H\alpha$ emission, we derive gas-phase metallicities from the $N2$ index, the ratio of $[N\text{ II}]\ \lambda 6583$ to $H\alpha$ emission line fluxes. We note a number of known concerns related to this metallicity indicator: contribution of AGN and shock ionization to the $[N\text{ II}]$ emission (further addressed in Section 3.1), saturation at high metallicities, variations in the N/O ratio and secondary nitrogen production, and contribution of the warm diffuse ISM. Given these possible biases, we show our results in terms of the observed $[N\text{ II}]/H\alpha$ ratio. When a conversion to metallicity is required for a comparison to the literature, the linear conversion by Pettini & Pagel (2004) is used, $12 + \log(O/H) = 8.9 + 0.57 \times \log([N\text{ II}]/H\alpha)$. This carries a systematic uncertainty of 0.18 dex.

3. THE MASS–METALLICITY RELATION

We create an integrated 1D spectrum for each galaxy by co-adding all the spatial pixels within the mask after velocity-

shifting each spatial pixel to remove the imprint of the overall galaxy kinematics. The $H\alpha$ and $[N\text{ II}]$ emission lines are jointly fit with a three-component Gaussian model, forcing a common redshift and line width, and constraining the $[N\text{ II}]\ \lambda 6583/[N\text{ II}]\ \lambda 6548$ doublet ratio to its theoretical value of 3.071 (Storey & Zeippen 2000). Uncertainties are derived via a Monte Carlo approach where the spectrum is perturbed following its noise spectrum. From these fits we derive $H\alpha$ -based SFRs, corrected for dust extinction using the SED-derived reddening and accounting for additional extinction of the nebular lines following Wuyts et al. (2013). These agree to within a median scatter of 50% with the photometrically derived SFR estimates. The agreement is particularly sensitive to the availability of far-IR fluxes; a thorough comparison between both SFR indicators will be the subject of future work. The integrated $[N\text{ II}]$ emission is detected at $>3\sigma$ for 90% of the sample; $[N\text{ II}]/H\alpha$ ratios are reported in Table 3 in the Appendix.

3.1. AGN Contamination

It is well known that the $[N\text{ II}]$ emission can be contaminated by the ionizing spectrum of an AGN. There are a number of different AGN indicators in use in the literature, all of which suffer from biases and incompleteness. The “classical” indicators include X-ray emission, radio emission, and mid-IR colors. Keeping in mind that the coverage and depth of the various surveys vary across the CANDELS fields (see Genzel et al. 2014, for more details), we find a typically low percentage of 7% AGNs in our KMOS^{3D} sample. Surveys that also target $[O\text{ III}]$ and $H\beta$ emission can use the optical BPT diagnostic diagram (Baldwin et al. 1981) to identify the presence of AGNs in their sample, and typically find another $\sim 10\%$ contamination (Zahid et al. 2014; Sanders et al. 2015). The KMOS^{3D} survey currently does not cover the $[O\text{ III}]$ or $H\beta$ line for the majority of its targets, but $[N\text{ II}]/H\alpha$ alone also serves as a useful diagnostic to identify AGNs from rest-frame optical emission lines at high redshift (Stasińska et al. 2006; Cid Fernandes et al. 2011; Coil et al. 2015). We find that 8% of targets in our sample lie above a threshold $[N\text{ II}]/H\alpha > 0.6$, using the threshold from Kewley et al. (2001).

The spatially resolved integral field unit (IFU) data give access to two additional AGN indicators. The AGN contribution to the line emission is expected to be largest in the

Table 1
Stacked Mass–Metallicity Relation in Three Redshift Intervals,
with and without AGNs

Redshift	All		No AGN	
	$\log(M_*/M_\odot)$	[N II]/H α	$\log(M_*/M_\odot)$	[N II]/H α
$z \sim 0.9$	9.88	0.186 ± 0.026	9.91	0.218 ± 0.043
	10.17	0.250 ± 0.065	10.25	0.277 ± 0.044
	10.42	0.338 ± 0.068	10.55	0.364 ± 0.072
	10.58	0.436 ± 0.049	10.80	0.384 ± 0.038
	10.75	0.404 ± 0.067		
$z \sim 1.5$	10.96	0.432 ± 0.122		
	9.92	0.165 ± 0.026	9.93	0.164 ± 0.034
	10.34	0.233 ± 0.040	10.61	0.262 ± 0.057
$z \sim 2.3$	10.99	0.368 ± 0.204		
	10.03	0.119 ± 0.016	10.03	0.114 ± 0.012
	10.23	0.122 ± 0.026	10.27	0.134 ± 0.024
	10.38	0.142 ± 0.017	10.43	0.165 ± 0.020
	10.56	0.211 ± 0.032	10.59	0.231 ± 0.034
	10.69	0.293 ± 0.062	10.83	0.328 ± 0.115
	10.93	0.351 ± 0.049		
	11.13	0.542 ± 0.400		

nuclear region of the galaxy, and possibly diluted by the emission from the outer disk. We therefore create a nuclear spectrum for each of our targets by co-adding only the central $0''.4$. The nuclear [N II]/H α ratio lies above 0.6 for an additional 5% of the sample. Second, Förster Schreiber et al. (2014) and Genzel et al. (2014) reported evidence for nuclear AGN-driven outflows of ionized gas based on the presence of a broad underlying component with FWHM = 500–2000 km s $^{-1}$ in the line profile of H α and the forbidden lines. We visually examine all nuclear spectra as described by Genzel et al. (2014) and find evidence of underlying broad emission for 27% of the sample analyzed in this paper. The incidence of each of the AGN indicators described above is a strong function of stellar mass, such that at $\log(M_*/M_\odot) > 10.9$, 70% of the sample satisfies one or more of the AGN indicators.

3.2. The Evolution of the Mass–Metallicity Relation

The KMOS 3D sample has a high detection rate of 90% for the galaxy-integrated [N II] emission, not unsurprising given the required depth to spatially resolve the H α emission. Nevertheless, we stack our galaxies in bins of stellar mass to robustly take into account the upper limits. Similarly to Wuyts et al. (2014), we use inverse variance weighting of continuum-subtracted, velocity-corrected, and H α -normalized integrated spectra. The line fluxes and uncertainties are derived as the jackknife mean and standard error and reported in Table 1. We aim for 15–20 targets per bin. Figure 2 shows the MZR for the stacked spectra with and without the AGNs identified in the previous section. The strong dependence of AGN incidence on stellar mass results in a loss of many of the highest-mass galaxies. However, in the overlapping mass regime at $\log(M_*/M_\odot) \lesssim 10.8$, both stacked relations are consistent within the uncertainties, suggesting that in this mass range the effect of the AGN contribution to the galaxy-integrated [N II] emission is limited. At higher masses, the integrated [N II]/H α ratios are often biased high.

The results are in excellent agreement with the MZR presented in Wuyts et al. (2014) based on the first-year KMOS 3D data, augmented with observations with SINFONI at the VLT and the long-slit near-IR spectrograph LUCI at the Large Binocular

Telescope on Mount Graham, Arizona. The latter two data sets are responsible for the extension to lower stellar masses, especially in K band. Further comparison to the literature at $z \sim 1.6$ is available from the FMOS survey, for 168 galaxies in the COSMOS field observed with the multi-object near-IR spectrograph FMOS on Subaru (Zahid et al. 2014; Silverman et al. 2015). The wide field of view surveyed includes many more very massive targets compared to KMOS 3D , but the lack of spatially resolved data limits the detection of AGN contributions, which could explain the somewhat higher abundances at the high-mass end, where we have shown AGNs to bias the [N II]/H α ratios high. Most high- z emission-line science has so far been carried out at $z \sim 2.3$, where the full suite of rest-frame optical diagnostic lines can be observed in the near-IR wavelength range. The MZR presented by Erb et al. (2006) was long the only study with a large sample (~ 100) at this redshift, albeit with few individual [N II] detections. Recently, the new multi-object near-IR spectrograph MOSFIRE on Keck has changed the landscape with two large emission-line surveys of many hundreds of galaxies each. The MOSFIRE Deep Evolution Field (MOSDEF) survey follows a similar target selection to KMOS 3D in the 3D-*HST* CANDELS fields observable from Mauna Kea (Kriek et al. 2015). The Keck Baryonic Structure Survey (KBSS) targets 15 quasar fields with a large sample of spectroscopically confirmed redshifts at $1.5 \lesssim z \lesssim 3.5$ and a wealth of multi-wavelength ancillary data (e.g., Steidel et al. 2004, 2014; Rudie et al. 2012). We have taken care to consistently compare relations that have been derived with the same $N2$ indicator and linear Pettini & Pagel (2004) conversion employed here. Our results are in perfect agreement with the MOSDEF relation (Sanders et al. 2015), which is reassuring given our almost identical parent sample. The MZR relation reported by KBSS has a shallower slope, which is likely due to differences in the selected target population (A. Strom et al. 2016, in preparation).

As mentioned in the introduction, the evolution of metallicity at a given mass can be used to constrain key parameters in galaxy evolution models such as star formation efficiency (Lilly et al. 2013; Onodera et al. 2016) and gas recycling (Davé et al. 2011; Yuan et al. 2013b). In Figure 3 we show the metallicity evolution for three redshift bins ($z \sim 0.9, 1.5, 2.3$) and two stellar mass bins ($\log(M_*/M_\odot) = 10.0, 10.6$) for the KMOS 3D Survey. A steady evolution of [N II]/H α with comparable slope is observed in the two mass bins from $z = 2.7$ to 0.6. In the left panel we show the metallicity evolution of KMOS 3D galaxies in the context of other data in the literature. KMOS 3D and literature values are all recalibrated to the same metallicity system using Maiolino et al. (2008; see also Onodera et al. 2016). In the right panel we include the expected metallicity evolution derived using the Lilly et al. (2013) equilibrium model with an observationally motivated evolution of depletion time, $\epsilon \propto (1+z)^{0.43}$, from Genzel et al. (2015) with updated parameters from S. Wuyts et al. (2016, in preparation). The model, calibrated on the local “fundamental” relation (FMR; Mannucci et al. 2010), underpredicts the metallicity measurements from KMOS 3D but correctly traces the magnitude of metallicity evolution (gray shaded area). If both the normalization and $(1+z)$ evolution are adopted from Genzel et al. (2015) in place of Equation (38) of Lilly et al. 2013, then the metallicity evolution produced by the model is consistent with our KMOS 3D data but underpredicts the metallicity locally (dashed shaded area). KMOS 3D uniquely contributes [N II]/H α

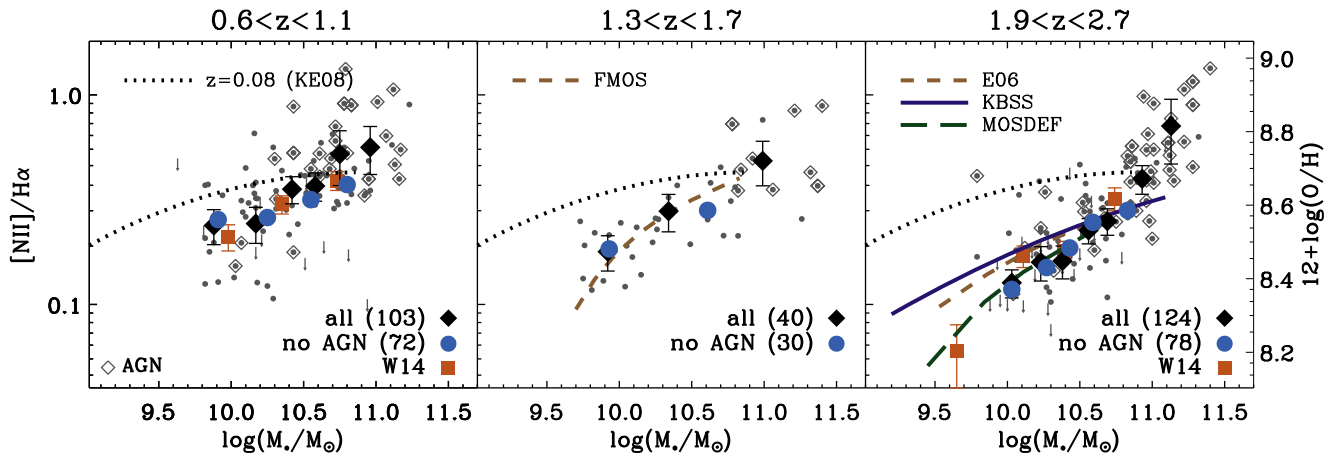


Figure 2. Galaxy-integrated $[\text{N II}]/\text{H}\alpha$ ratios as a function of stellar mass for the $\text{KMOS}^{3\text{D}}$ sample. The right axis expresses galaxy abundance as $12 + \log(\text{O}/\text{H})$ as derived from the linear relation by Pettini & Pagel (2004). The gray data points in the background show our individual detections and upper limits; AGNs are surrounded by an open diamond. The large black diamonds and blue circles correspond to the stacked spectra with and without AGN-identified targets, respectively. The local relation from Kewley & Ellison (2008) is shown with a dotted line in each panel. The orange squares correspond to the earlier $\text{KMOS}+\text{SINFONI}+\text{LUCI}$ results from Wuyts et al. (2014). Other studies in the literature include the FMOS survey at $z \sim 1.6$ (Zahid et al. 2014; brown dashed), and at $z \sim 2.3$ the sample from Erb et al. (2006; brown dashed), the KBSS survey (Steidel et al. 2014, dark blue dot-dashed), and the MOSDEF survey (Sanders et al. 2015; dark green dashed). Their MZR relations are represented consistently based on metallicities derived from the $N2$ indicator and the linear Pettini & Pagel (2004) conversion.

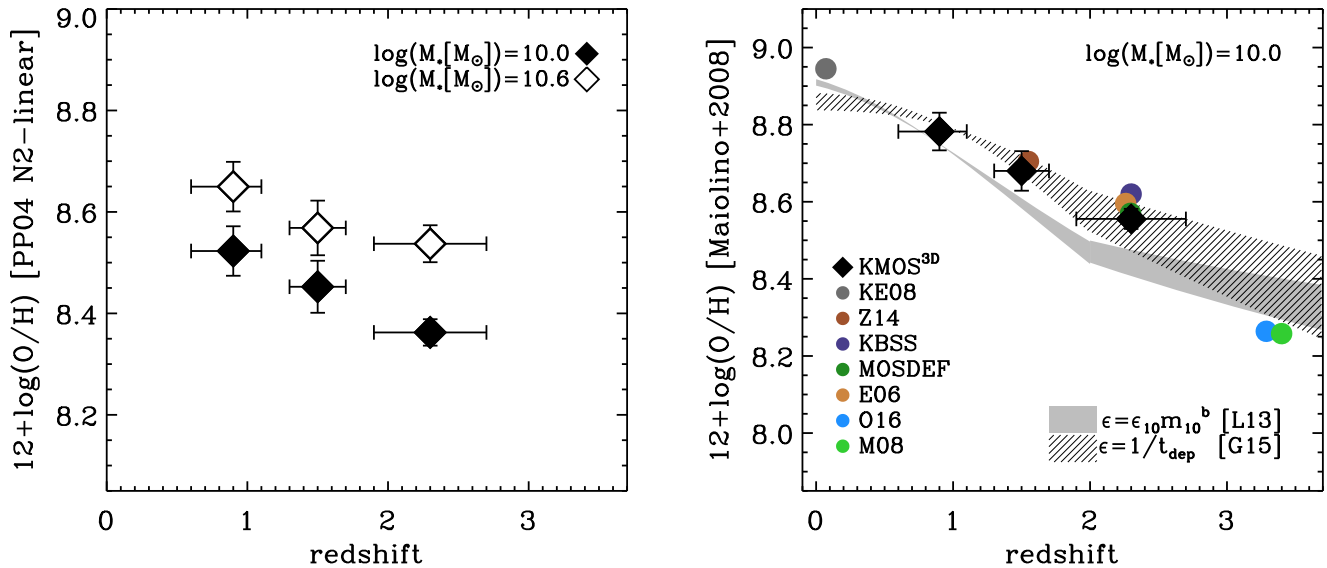


Figure 3. Cosmic metallicity evolution for massive galaxies. Left: Evolution of metallicity as determined by the $[\text{N II}]/\text{H}\alpha$ abundance ratio (excluding AGNs) within the $\text{KMOS}^{3\text{D}}$ data in mass bins of $M_* = 10^{10} M_\odot$ (filled symbols) and $M_* = 10^{10.6} M_\odot$ (open symbols). In the right panel we show $\text{KMOS}^{3\text{D}}$ in the context of other relevant measurements (Kewley & Ellison 2008; Maiolino et al. 2008; Henry et al. 2013; Cullen et al. 2014; Steidel et al. 2014; Zahid et al. 2014; Sanders et al. 2015; Onodera et al. 2016). $\text{KMOS}^{3\text{D}}$ and literature data are recalibrated to the same metallicity system using Maiolino et al. (2008; see also Onodera et al. 2016). The gray band shows the expected metallicity evolution following the equilibrium model of Lilly et al. (2013), fit to the local FMR of Mannucci et al. (2010), with an evolving star formation efficiency from Genzel et al. (2015), $\epsilon \propto (1+z)^{0.34 \pm 0.15}$. The width of the band spans $0 < Z_0/y < 0.1$, where Z_0 is the metallicity of incoming gas and y is the chemical yield (Lilly et al. 2013). The hashed band shows the predicted metallicity evolution when the full equation for star formation efficiency is adopted from Genzel et al. (2015) in place of Equation (38) of Lilly et al. (2013).

measurements for consistent sample selection, data quality, and methods across 6 Gyr allowing a stronger constraint on evolutionary models.

3.3. The Effect of Star Formation Rate

In the local universe, Ellison et al. (2008) first reported an anticorrelation between metallicity and specific SFR (sSFR). Further studies showed how including the SFR as a second parameter in the MZR reduces the scatter (Mannucci et al. 2010; Andrews & Martini 2013). There have been claims that FMR between stellar mass, SFR, and galaxy abundance is independent of redshift, such that the lower abundances observed

at high redshift at fixed stellar mass are fully explained by the overall higher SFR at these epochs (e.g., Mannucci et al. 2010; Belli et al. 2013; Henry et al. 2013; Stott et al. 2013). However, the majority of high- z studies report no dependence of the MZR on SFR, or an offset from the local FMR (Steidel et al. 2014; Troncoso et al. 2014; Wuyts et al. 2014; Zahid et al. 2014; Grasshorn Gebhardt et al. 2015; Sanders et al. 2015). Salim et al. (2015) present evidence for a (noisy) SFR dependence and for the existence of an FMR only at intermediate stellar masses, where such a dependence exists locally as well.

Our data do not show a significant trend between inferred metallicity and sSFR, irrespective of whether we use dust-

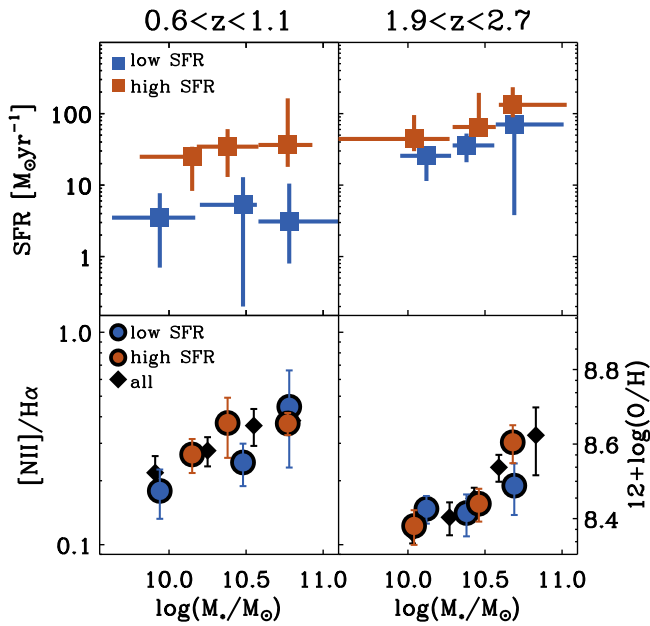


Figure 4. Effect of star formation on metallicity, using the dust-corrected SFRs derived from the integrated $H\alpha$ flux. Top panels show the median value and range of a low- and high-SFR bin for three stellar mass bins at $z \sim 0.9$ and $z \sim 2.3$. The MZR for the low- and high-SFR bins separately is shown in the bottom panels, and compared to the MZR for all galaxies from Figure 2. There is no significant offset between the SFR bins.

corrected $H\alpha$ -based SFRs or photometrically derived SFRs. This is in contrast to recent results from the KMOS Redshift One Spectroscopic Survey (KROSS; Magdis et al. 2016), which are based on dust-corrected $SFR_{H\alpha}$ estimates with the same recipe for extinction. A possible cause lies in the less complete removal of AGN contamination from the KROSS sample, as well as a difference in survey depth at $z \sim 1$ (KMOS^{3D}: ~ 5 hr; KROSS: ~ 2.5 hr). To investigate the dependence on SFR at fixed mass and redshift, we split our AGN-excluded sample at $z \sim 0.9$ and $z \sim 2.3$ into two bins of SFR, using the dust-corrected SFRs derived from the integrated $H\alpha$ flux (Figure 4). The intermediate-redshift bin at $z \sim 1.5$ does not yet contain sufficient targets. We do not see a significant offset between the MZR separately derived for the low- and high-SFR bins. This does not change when we use the photometrically based SFR estimates from UV+IR broadband data. The dynamic range of the $z \sim 2.3$ sample is very limited, but over the SFR range probed at $z \sim 0.9$ in KMOS^{3D}, a significant effect on metallicity is seen in the local universe (Andrews & Martini 2013).

The equilibrium or “gas-regulator” picture of galaxy evolution driven by the balance between gas accretion, star formation, and gas outflow naturally finds an FMR between stellar mass, SFR, and metallicity (e.g., Lilly et al. 2013). Although the redshift evolution of metallicity inferred from our $[NII]/H\alpha$ measurements appears in good agreement with predictions from the Lilly et al. model (see Figure 3), the lack of observed correlation between metallicity and SFR at fixed z and stellar mass remains puzzling and could signify departures from the first-order assumptions of these simple analytical equilibrium models. First, however, the possible caveats related to metallicity measurements based on strong-line indicators should be more completely understood.

4. ABUNDANCE GRADIENTS

The spatial distribution of the $[NII]/H\alpha$ ratio across individual galaxies contains additional information beyond a simple measurement of the galaxy-integrated abundance. For each target, a set of elliptical annuli is created, centered on the continuum light, angled along the kinematic position angle (see Wisnioski et al. 2015) and with an ellipticity matching the outer $H\alpha$ contours. Given the FWHM of our seeing-limited data, we ideally choose apertures with a width of $0''.4$, or 2 spatial pixels. However, only 40% of the sample has enough S/N over a large enough area to detect $[NII]$ at $>3\sigma$ in three subsequent 2 pixel wide apertures, which is our requirement to robustly measure a radial gradient. Especially in the highest-redshift bin at $z \sim 2.3$, most galaxies are too small and for only 17% can a gradient be measured. Therefore, our default apertures have a width of $0''.2$. Where possible, we have checked that gradients measured with $0''.2$ and $0''.4$ wide apertures are consistent within the uncertainties. In each aperture, we create a velocity-corrected integrated spectrum and jointly fit the $[NII]$ and $H\alpha$ emission as described in Section 3. A linear fit of the $[NII]/H\alpha$ ratio as a function of the semimajor axis radius (defined in the middle of each annulus) results in a measurement of the gradient $\Delta N2/\Delta r$ in dex kpc^{-1} . Figure 11 in the Appendix shows the $H\alpha$, velocity, and $[NII]/H\alpha$ map, as well as the $[NII]/H\alpha$ ratio as a function of radius for five example galaxies to illustrate the process. We have visually examined each gradient measurement to avoid catastrophic failures in the fit.

For the galaxies identified as having some AGN contribution from one of the indicators described in Section 3.1, the $[NII]$ emission in the central region could be enhanced by the AGNs and thus not accurately represent the metallicity of the ionized gas. In these cases, we exclude the inner two apertures (i.e., the inner $0''.4$) from the radial fit. When only four apertures with robust $[NII]$ detections exist, only the innermost aperture is excluded. For these targets, removing two apertures and fitting a gradient to only the remaining outer two radial bins gives consistent results. AGNs with only three radial $[NII]$ detections are excluded. For the full sample of AGNs, the restricted gradients are on average 0.001 ± 0.02 dex kpc^{-1} flatter, i.e., fully consistent with the full radial gradients, as can be seen in Figure 5.

The final gradient measurements are reported in Table 3 in the Appendix. Most of the observed gradients are flat; only 15/180 targets exhibit a gradient significantly offset from zero (at $>3\sigma$), of which 13 gradients are negative and 2 positive. Figure 6 shows the full sample of measured gradients as a function of stellar mass in $[dex kpc^{-1}]$ and $[dex/r_e]$ in the top and bottom panels, respectively, color-coded by redshift. Based on a sequence of 1000 Spearman correlation tests, where we randomly vary the sample of gradients according to their uncertainties, the negative correlation with stellar mass is significant at 2.8σ . We find a positive correlation with sSFR at 2.5σ ; the significance reduces to 1.5σ when the sSFR is normalized to the main sequence at each redshift. Stott et al. (2014) have similarly reported a weak positive trend with sSFR at 2.9σ , explained through the inflow of metal-poor gas flattening the gradients of strongly star-forming systems. No significant correlations are present with integrated $[NII]/H\alpha$ or any of the dynamical (dispersion, velocity gradient, v_{obs}/σ_0) or structural (effective radius, inclination) properties of the galaxies.

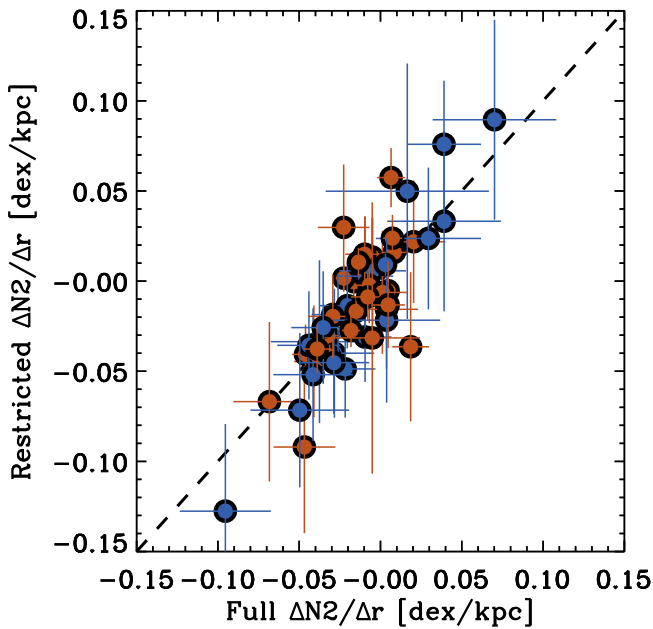


Figure 5. Comparison of the full radial gradient with the gradient restricted to the outer disk for the galaxies flagged as AGNs. For the orange symbols, the inner $0''.4$ covered by the two innermost apertures is excluded from the fit; for the blue symbols we can exclude only the innermost $0''.2$ to keep at least three radial [N II] detections. The uncertainties for the restricted gradient on the y-axis are naturally larger due to the fewer radial data points, but on average the AGN does not significantly steepen the derived linear gradient.

Ho et al. (2015) have recently reported steeper gradients for lower-mass galaxies at 3.4σ significance for a sample of 49 local field galaxies, the opposite trend from what we find here for KMOS^{3D}. The uncertainties and scatter in the abundance gradient measurement in their low-mass bin of $\log(M_*/M_\odot) = 8-9$ increase greatly. Observationally, gradient measurements at high redshift are affected more by uncertain AGN contamination or shock ionization, more prevalent at the high-mass end, as well as beam smearing effects limiting our resolution more strongly for the lower-mass, smaller sources. Given these considerations and the limited statistical significance of both our trend and the trend seen by Ho et al. (2015) with stellar mass, we choose to refrain from further investigation of possible underlying physics related to the different trends at low and high redshift at this point.

4.1. Beam Smearing

Before physically interpreting the observed gradients, it is crucially important to understand the effects of the coarse spatial resolution of seeing-limited data on the intrinsic abundance gradients of high-redshift galaxies. For this purpose we have analyzed a set of exponential disk models created with the IDL code DYSMAL (Cresci et al. 2009; Davies et al. 2011) for a range of inclination and effective radius. We add [N II] emission assuming a smooth linear radial gradient with a chosen central [N II]/H α ratio and slope. The model cubes are convolved with a Gaussian PSF for a range of assumed FWHM from $0''.1$ for some AO-assisted data to $1''.0$ for seeing-limited data taken in bad observing conditions, and random noise is added to achieve a pre-defined S/N for the central pixel. Table 2 summarizes the default value (in bold) and explored range for each parameter, chosen to reflect the range of properties found in the KMOS^{3D} sample. All model cubes are

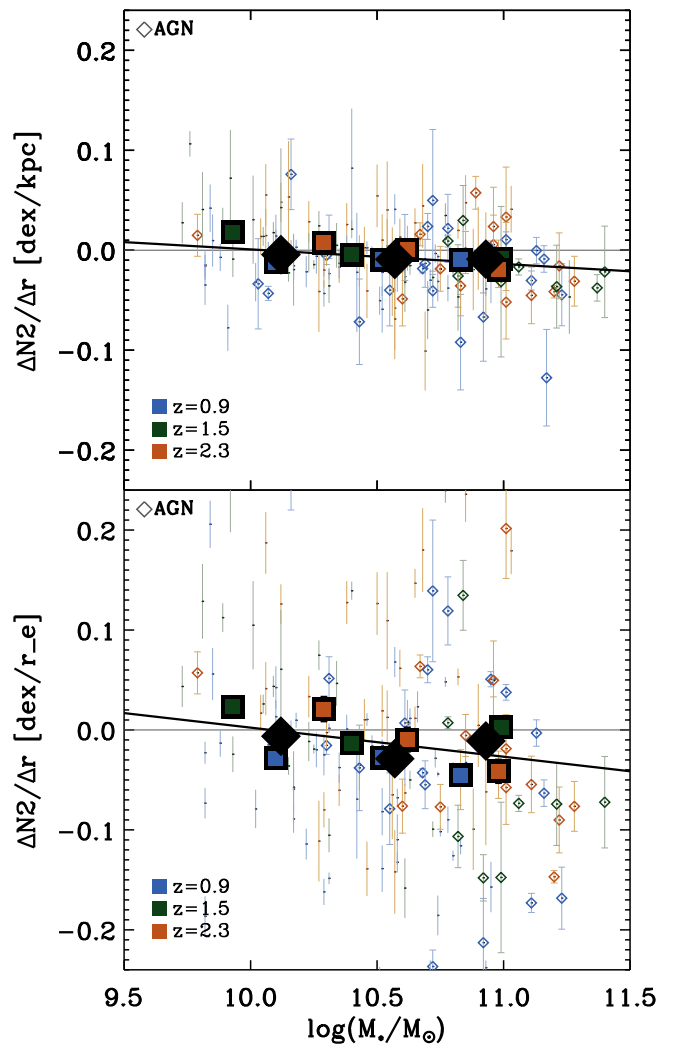


Figure 6. Observed metallicity gradients as a function of stellar mass, color-coded by redshift. The top panel shows gradients in $[\text{dex kpc}^{-1}]$; in the bottom panel they have been normalized to the effective radius. Targets surrounded by an open diamond are flagged as AGNs by one of the indicators described in Section 3.1. The large squares correspond to the weighted average gradient in three bins of stellar mass for each redshift; the black diamonds show the weighted average for the full sample. The black line is a simple 1D fit to those points. From a sequence of 1000 Spearman correlation tests, randomly varying the sample around the uncertainties, this trend is significant at 2.8σ in both panels.

Table 2

Parameters Used for Model Data Cubes to Explore Beam-smearing Effects	
Parameter	Value
FWHM (arcsec)	0.1, 0.2, 0.3, 0.4, 0.5, 0.6 , 0.7, 0.8, 0.9, 1.0 + AO
r_e (arcsec)	0.3, 0.4, 0.5 , 0.6, 0.7, 0.8, 0.9, 1.0
Inclination (deg)	0, 30, 45 , 60, 75
S/N _{central}	10, 20 , 30
[N II]/H α _{central}	0.3, 0.5 , 1.0
Gradient (dex kpc ⁻¹)	0.2, 0.1, 0.05, -0.05, -0.1 , -0.2

analyzed in the exact same way as described in Section 4 for the KMOS data.

From this first-order analysis, we find that the beam smearing mainly depends on the ratio of the FWHM of the data to the effective radius of the galaxy, which determines how well it can be resolved radially. The right panel of Figure 7

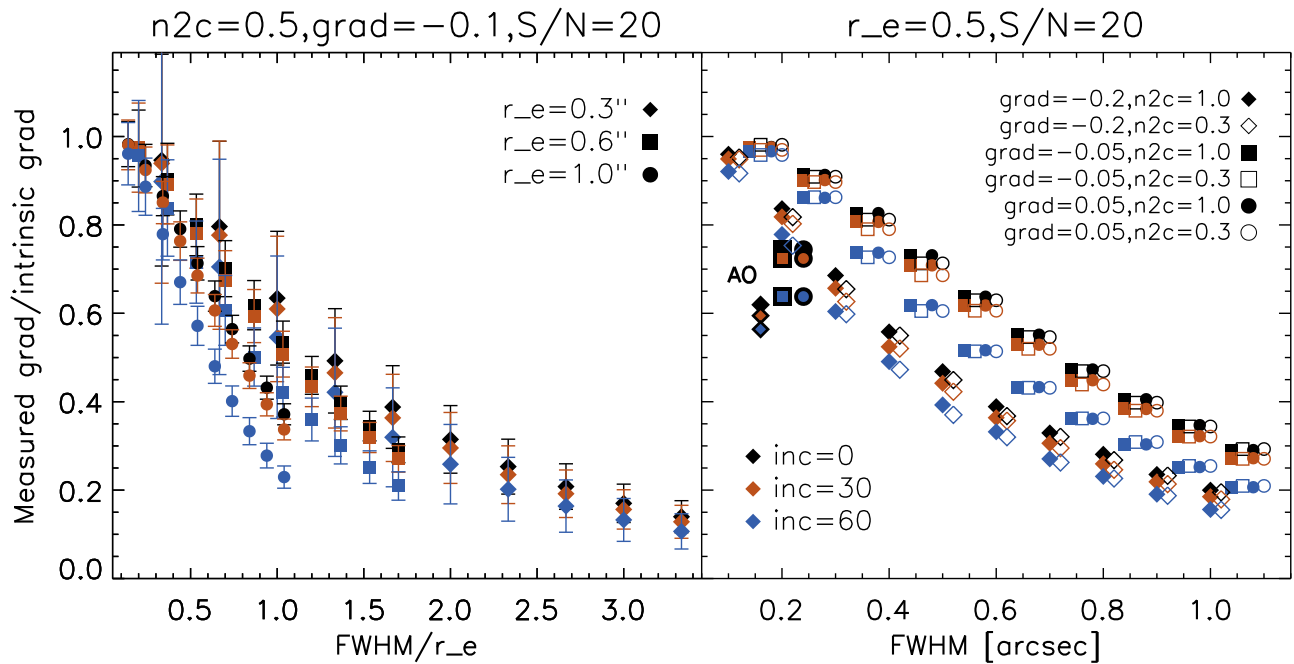


Figure 7. Ratio of the recovered vs. intrinsic radial $\Delta N_2/\Delta r$ gradient for our set of exponential disk models assuming a linear smooth intrinsic abundance gradient. The color-coding in both panels shows a range of inclinations from face-on ($\text{inc} = 0^\circ$) to almost edge-on ($\text{inc} = 60^\circ$). In the left panel, the x -axis represents the FWHM of the observations divided by the effective radius for $r_e = 0''.3$, $0''.6$ and $1''.0$. The other parameters (central $[\text{N II}]/\text{H}\alpha$ value $[n2c]$, intrinsic gradient $[\text{grad}]$, and S/N) are kept at their default values as specified in Table 2. The ratios have all been derived at the same discretized set of input FWHM, but to improve the clarity of the figure, we have shifted the data points for different effective radii slightly along the x -axis. Gradients are more affected by beam smearing for larger ratios of seeing vs. galaxy size. The right panel compares the ratio of the recovered vs. intrinsic gradient as a function of the FWHM of the observations for different intrinsic gradients and central $[\text{N II}]/\text{H}\alpha$ ratios. In this panel the effective radius is kept fixed at its default value of $0''.5$. The positions along the x -axis have similarly been shifted to improve the clarity of the figure. A shallower intrinsic gradient is less affected by beam smearing, while the central N_2 ratio has no impact. The black-edged symbols shown at $\text{FWHM} \sim 0''.16$ correspond to the double-component PSF of SINFONI+AO data.

additionally shows that more highly inclined galaxies and intrinsically steeper gradients are each affected more, as would be expected. The central $[\text{N II}]/\text{H}\alpha$ ratio does not matter, as long as one has enough sensitivity to detect $[\text{N II}]$ in the outer disk. And finally, the S/N of the central pixel only impacts the uncertainties, as was also found by Yuan et al. (2013a).

The KMOS^{3D} data are taken under mostly uniform seeing conditions ($\text{FWHM} = 0''.55 \pm 0''.09$). From our models, we see that we can recover at most 70% of the intrinsic gradient for the largest face-on disks, down to only $\sim 25\%$ in the smallest, highly inclined targets. To compare beam-smearing effects with AO-assisted data sets, we also ran simulations assuming the PSF properties of SINFONI+AO observations, for which the PSF is best characterized with a double-component Gaussian model to capture the AO-corrected narrow core component with $\text{FWHM} = 0''.16$ and 86% of the peak flux, and the uncorrected broad halo underneath with $\text{FWHM} = 0''.5$ and 14% of the peak flux (Förster Schreiber et al. 2009; Förster Schreiber et al. 2016, in preparation). The halo causes a larger beam-smearing effect than measured for a single-Gaussian FWHM of $0''.16$. On average, AO data recover 65% of the gradient, as opposed to 50% at seeing-limited resolution. Utilizing the *HST* grism capabilities as in Jones et al. (2015) delivers a single narrow PSF at $\text{FWHM} \sim 0''.2$ and allows the most accurate gradient measurement.

Two previous efforts to take into account the effects of beam smearing have been made. Yuan et al. (2013a) simulate high- z data cubes with different seeing and S/N values based on the measured central abundance and abundance gradient for one specific local galaxy (IRAS F17222-5953) and recover only 13% of the intrinsic gradient when using three uniform radial

bins at $\text{FWHM} = 0''.6$. For the KMOS observations of 20 HiZELS galaxies at $z = 0.8$, Stott et al. (2014) perform a simulation of 1000 disk galaxies with a range of inclinations and input gradients and recover 80% of the intrinsic gradient in a face-on disk at $0''.7$ seeing. For an inclination of 80° , this reduces to 30%. This is in contrast to our results, which only recover 35% at $\text{FWHM} = 0''.7$ and are much less dependent on inclination. It remains unclear from where this difference arises. From our analysis, a large dependence on inclination is unexpected, since the use of elliptical apertures along the major axis following the axis ratio of the $\text{H}\alpha$ contours is designed to mostly take this into account.

Under the assumption that we know the effective radius and inclination of each KMOS^{3D} target from GALFIT modeling of the F160W CANDELS photometry (van der Wel et al. 2012), and that the line emission mostly follows the stellar light as traced by the F160W continuum, we can derive the necessary beam-smearing correction from our set of models. Figure 12 in the Appendix visualizes how this is done for three examples. For a known combination of FWHM, inclination, and effective radius, a certain intrinsic gradient will be beam-smearred into a unique observed gradient. We derive this match for a range of intrinsic gradients between -0.2 and 0.2 dex kpc^{-1} for each target and then simply invert this correlation to derive the intrinsic gradient that corresponds to the actual observed gradient of the target. A histogram of the resulting beam-smearing correction factors and corrected gradients for the full sample is shown in Figure 8. We caution that each corrected gradient in this histogram has large uncertainties. We re-investigate correlations between the now-intrinsic gradients and the stellar population, structural, and kinematic parameters and

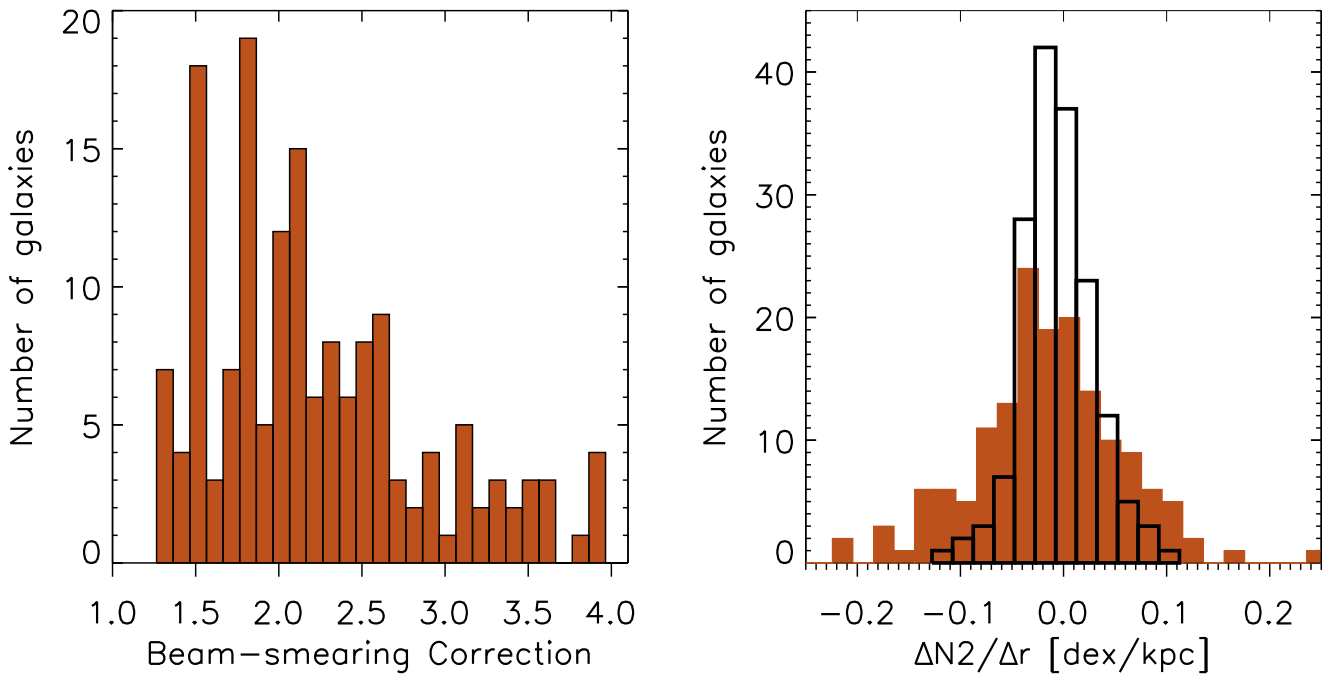


Figure 8. Left: histogram of the required beam-smearing corrections for the 180 gradients measured in the KMOS^{3D} sample, under the simple assumption of a linear smooth intrinsic gradient as discussed in the text. The corrections are based on the relevant seeing and the effective radius and inclination of the targets as derived from GALFIT modeling of the F160W CANDELS photometry. Right: histograms of observed (black) and intrinsic (filled orange) $\Delta N_2/\Delta r$ gradients.

again do not find any statistically significant trends. Finally, we want to emphasize that these corrections are derived under the assumption of a smooth, linear radial gradient. Given the clumpy nature and often irregular morphology of high-redshift star-forming galaxies (SFGs), this presents a simplification. Mock observations of simulated galaxies provide a better approach; this will be explored in more detail in future work.

4.2. Gradients in Interacting Systems

In the local universe, galaxies undergoing an interaction show flattened gradients (e.g., Kewley et al. 2010; Rupke et al. 2010b; Sánchez et al. 2014). This is expected from simulations, as the interaction causes inflows of metal-poor gas from the outskirts into the galaxy center (Rupke et al. 2010b). Torrey et al. (2012) differentiated in their simulations between low and high gas fraction disks. While low gas fraction systems showed a depression in nuclear metallicity of ~ 0.07 dex, a slight enhancement in nuclear metallicity was found for systems with high gas fractions caused by the competing effect of enhanced nuclear star formation activity. Due to time delays between the occurrence of this enhanced SF and the development of tidal inflows, the merger stage at the time of observations plays an important role in the effect on the nuclear metallicity (Perez et al. 2011). At high redshift, the observational evidence remains inconclusive. For their samples of lensed galaxies, Jones et al. (2013) and Leethochawalit et al. (2015) report shallower gradients for the merging or dynamically disturbed systems. Similarly, four out of the seven galaxies with a positive abundance gradient in the seeing-limited MASSIV sample at $z \sim 1.2$ are interacting (Queyrel et al. 2012). In contrast, Cresci et al. (2010) and Troncoso et al. (2014) find positive gradients in rotating disks, which would require the inflow of metal-poor gas into the galaxy center through minor mergers, cold flows, or violent disk instabilities (e.g., Dekel & Burkert 2014; Zolotov et al. 2015).

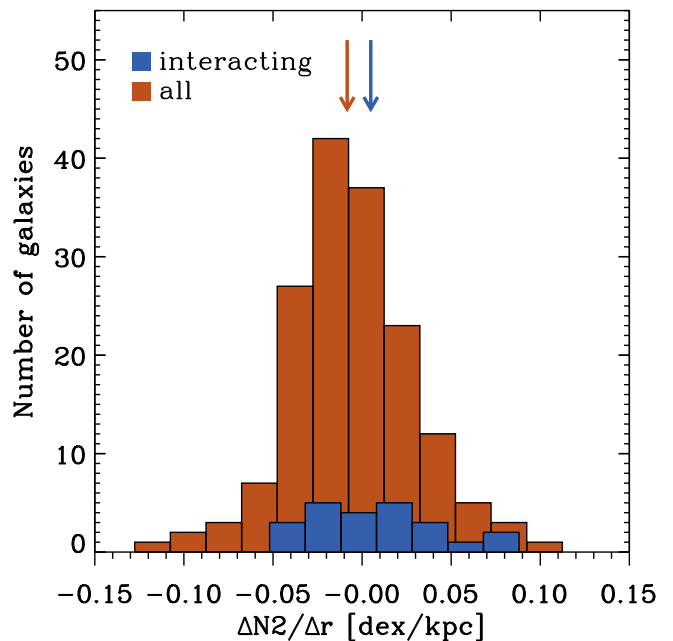


Figure 9. Comparison of the full sample of KMOS^{3D} $\Delta N_2/\Delta r$ gradients in orange vs. the 23 interacting systems in blue. The difference is not statistically significant. The orange and blue arrows indicate the median gradient of -0.008 ± 0.003 and 0.005 ± 0.008 for the full sample and pairs, respectively. Given the uncertainties, the interacting systems do not show significantly flatter gradients.

Within the KMOS^{3D} sample, we find only a handful of galaxies with a statistically significant positive gradient. Wisnioski et al. (2015) define a sample of pairs based on a search for companions in the 3D-*HST* catalog with a velocity separation of 500 km s^{-1} , expected to fall within the IFU of the primary target—this roughly translates to a projected separation

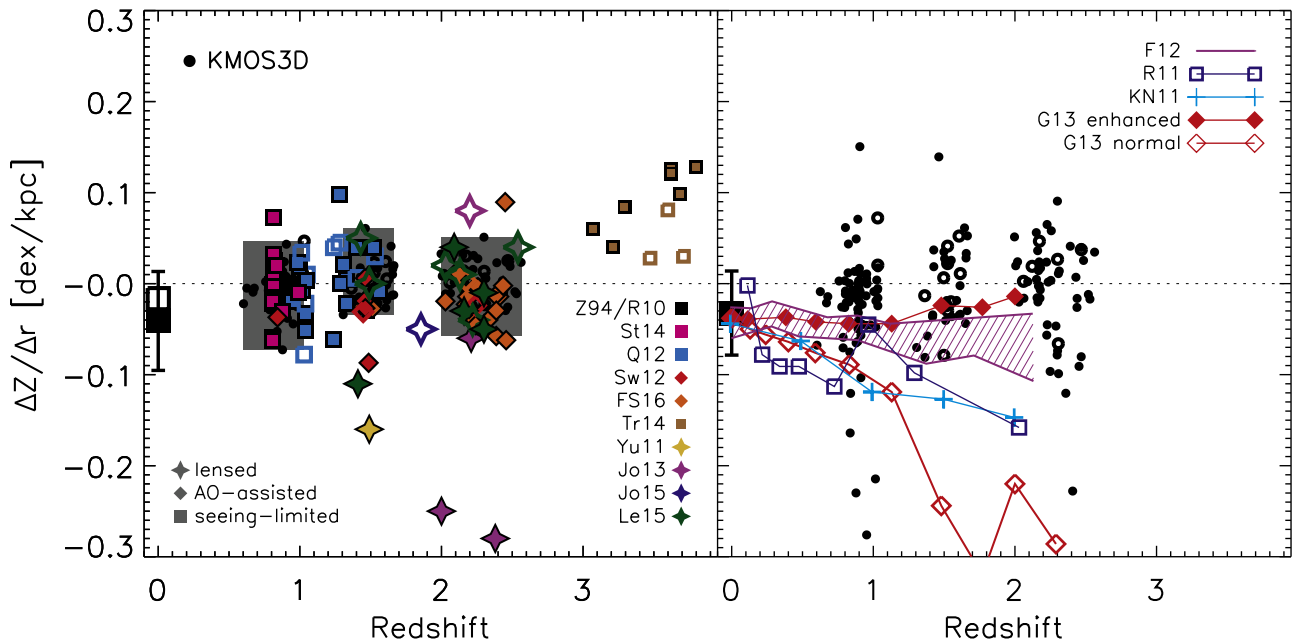


Figure 10. Left: compilation of the KMOS^{3D} results with all the abundance gradients measured at high redshift from the literature. Open symbols refer to interacting or disturbed systems, as defined in the various papers. In the local universe, the filled and open black squares shows the median gradient for a sample of isolated spiral galaxies (Zaritsky et al. 1994; Rupke et al. 2010b) and interacting spiral systems (Rupke et al. 2010b), respectively. The star symbols refer to gravitationally lensed galaxies (Yuan et al. 2011; Jones et al. 2013, 2015; Leethochawalit et al. 2015); diamonds have AO-assisted data (Swinbank et al. 2012, Förster Schreiber et al. 2016, in preparation); squares have only seeing-limited data (Queyrel et al. 2012; Stott et al. 2014; Troncoso et al. 2014). KMOS^{3D} data are represented by small black open or filled circles. To aid visibility, the gray background squares indicate the spread of the KMOS^{3D} measurements in the three redshift intervals. In the right panel, the KMOS^{3D} galaxies have been corrected for the effect of beam smearing. We additionally plot different theoretical predictions for the time evolution of abundance gradients from Pilkington et al. (2012) based on simulations in Rahimi et al. (2011), Kobayashi & Nakasato (2011), Few et al. (2012), and Gibson et al. (2013).

of $1''.5$ or 12 kpc. There are 39 such targets in the sample, for which we can recover 18 gradients. Additionally, one of the companion galaxies is sufficiently detected and extended for an additional gradient measurement. We also extend our definition of pairs to the more commonly used projected separation <50 kpc (restricted to spectroscopic redshifts) and classify four additional KMOS^{3D} targets with a gradient measurement as interacting, for a total sample of 23. Figure 9 compares the 23 gradients in interacting systems to the full KMOS^{3D} sample. The median gradient of 0.005 ± 0.008 (standard deviation 0.036) is not significantly flattened compared to the full median of -0.008 ± 0.003 (standard deviation 0.035). A Kolmogorov–Smirnov (K-S) test indicates a likelihood of 29% that both sets originate from the same parent sample. When first applying the beam-smearing correction, we find 0.011 ± 0.016 (standard deviation 0.08) for the pairs and -0.015 ± 0.008 (standard deviation 0.10) for the full sample, with a K-S test likelihood of 31%.

From scaling relations, we expect high gas fractions of on average 50% for the KMOS^{3D} sample (Tacconi et al. 2013; Genzel et al. 2015). The unknown merger stage for our sample of pairs makes it difficult to predict whether we should see an effect on the abundance gradients based on the simulations. Additionally, the predicted effects are small and remain difficult to distinguish given the relatively large errors on our gradient measurements, as well as the beam-smearing uncertainty.

4.3. Evolution of Metallicity Gradients with Cosmic Time

Figure 10 compiles available abundance gradients from the literature as a function of redshift. For this compilation, we convert our gradients in $[\text{N II}]/\text{H}\alpha$ ($\Delta N_2/\Delta r$) into abundance

gradients $\Delta Z/\Delta r$ by multiplying by a factor of 0.57 in accordance with the linear conversion by Pettini & Pagel (2004). In the local universe, the median gradient for a sample of isolated spiral galaxies from Rupke et al. (2010b) and Zaritsky et al. (1994) is -0.04 ± 0.05 dex kpc^{-1} . The open square symbol shows the flatter gradient of -0.0165 dex kpc^{-1} for galaxies currently undergoing an interaction (Rupke et al. 2010b). These studies use the R_{23} metallicity indicator of $([\text{O II}] \lambda\lambda 3727, 3729 + [\text{O III}] \lambda 4959 + [\text{O III}] \lambda 5007)/\text{H}\beta$. Rupke et al. (2010b) compare their results to abundances calculated from $[\text{N II}] \lambda 6583/[\text{O II}] \lambda\lambda 3727, 3729$ and $([\text{O III}] \lambda 5007)/\text{H}\beta/([\text{N II}] \lambda 6583/\text{H}\alpha)$ (the O3N2 indicator) and find no systematic difference after calibrating the different indicators following Kewley & Ellison (2008). At high redshift, abundance gradients are almost exclusively derived from the $[\text{N II}]/\text{H}\alpha$ ratio, since it only requires observations in one band and is insensitive to dust correction. Jones et al. (2013) and Leethochawalit et al. (2015) additionally measure O3N2 for a subset of their samples and find consistent results. The grism data from Jones et al. (2015) and the $z > 3$ sample from Troncoso et al. (2014) do not have access to $\text{H}\alpha$ and use the R23 diagnostic instead. For the literature sample in Figure 10, the star symbols correspond to lensed galaxies with AO, diamonds are nonlensed galaxies with AO, and squares show seeing-limited data. Open symbols show interacting or disturbed systems, as defined in the various papers from kinematic classification, visual inspection of broadband imaging, or a combination of both. For KMOS^{3D}, we use the pair classification as described above.

With the availability of larger samples, the steep abundance gradients found in lensed galaxies by Jones et al. (2013) and Yuan et al. (2011) that spurred much of the initial debate on the

feasibility of gradient measurements in field galaxies, as well as the idea of a strong flattening of gradients over cosmic time, now seem more like outliers. These lensed galaxies have lower stellar masses than typically targeted in the other surveys (the three steepest gradients in Figure 10 were measured for $\log(M_*/M_\odot) = 9.7$ and 9.9 [Jones et al. 2013] and a dynamical mass of $10.42M_\odot$ [Yuan et al. 2011]), but there is still overlap. The KMOS^{3D} survey, for example, probes down to $\log(M_*/M_\odot) = 9.7$, as can be seen in Figure 6. The uncertainty of beam-smearing corrections (Section 4.1) could still imply that the higher angular resolution of lensed studies remains a unique probe of intrinsically steep gradients. However, the larger study of lensed galaxies in Leethochawalit et al. (2015)—which applies the same methodology as Jones et al. (2013)—finds mostly flat gradients.

In the right panel of Figure 10, the KMOS^{3D} gradients are corrected for beam smearing. We cannot extend this correction to the literature data, since we do not always know the FWHM, effective radius, and inclination of the targets. Overplotted are models for the evolution of gradients over time from Rahimi et al. (2011), Kobayashi & Nakasato (2011), Few et al. (2012), and Gibson et al. (2013) as derived by Pilkington et al. (2012). The red open and filled diamonds compare the normal and enhanced feedback mode for the same simulation from Gibson et al. (2013). There is large scatter in the observed gradients, and remaining uncertainty with regard to the beam-smearing correction, but based on these models, the scarcity of gradients much steeper than $-0.1 \text{ dex kpc}^{-1}$ at $z \sim 2$ suggests the need for strong feedback.

5. SUMMARY AND DISCUSSION

This work takes advantage of the large sample size and wide redshift coverage of the KMOS^{3D} near-IR IFU survey to infer the integrated metal abundance and abundance gradient of star-forming galaxies at the peak of cosmic star formation activity between $z = 0.6$ and 2.6 from the $[\text{N II}]/\text{H}\alpha$ flux ratio. Such measurements can shed crucial light on the main physical processes driving the assembly of stellar mass and heavy elements in the universe. Our main conclusions are as follows:

1. Our MZR confirms previous literature results. Excluding AGN reduces sensitivity at the high-mass end, but does not significantly change the relation at lower masses ($\log(M_*/M_\odot) \lesssim 10.8$). We do not find a significant effect of SFR or sSFR on the observed $[\text{N II}]/\text{H}\alpha$ ratios.
2. A thorough analysis of the effect of beam smearing in seeing-limited data at high redshift shows that one can recover between 30% and 70% of the intrinsic abundance gradient, depending mostly on the ratio of the FWHM of the data to the effective radius, and to a lesser extent on galaxy inclination.
3. The majority of observed $[\text{N II}]/\text{H}\alpha$ gradients are flat. Cosmological simulations suggest the need for strong feedback to create flat abundance gradients at high redshift. No statistically significant correlations with stellar, kinematic, or structural galaxy properties are found.

A number of factors could cause intrinsically flat abundance gradients. One effect is the radial inflow of metal-poor gas and metal mixing caused by a merger. In the local universe, this has been established to cause shallower gradients, both observationally and in simulations (Rupke et al. 2010a, 2010b). At

high redshift, the merger fraction remains highly debated, with most observational results pointing to consistent or higher fractions than found locally (e.g., Lotz et al. 2008; Man et al. 2012; Lackner et al. 2014; López-Sanjuan et al. 2014). However, not all high- z surveys systematically find shallower gradients for disturbed systems, as discussed in Sections 4.2 and 4.3.

A second important physical process is feedback, which can blow out metal-rich gas from the center and redistribute it at larger radii. The ubiquitous presence of both AGN- and star-formation-driven feedback is well established at high redshift, especially at high mass and star formation surface density (e.g., Newman et al. 2012; Genzel et al. 2014).

Aside from these physical effects, one has to take into account the various reasons why the *observed* gradient could be flat. Beam-smearing is the most important factor here, and while we have attempted to address this, significant uncertainties remain. Second, in analogy with local SFGs, the fraction of warm diffuse ionized gas increases in radial apertures farther out in the galaxy disks and could strongly bias the measured line ratios there (Yuan et al. 2011). AO-assisted data reach the resolution of massive star-forming clumps at $z \sim 2$ and could thus minimize this effect, but the uncorrected seeing-limited halo still contributes to the beam-smearing correction (Figure 7). Space-based grism data are more suited, but struggle with sensitivity.

Similar biases are introduced when shock fronts alter the photoionization conditions of the interstellar medium (e.g., Kewley et al. 2013; Newman et al. 2014). These biases affect any abundance indicator based on rest-frame optical emission-line ratios, but have especially significant effects for the $N2$ indicator. Spatially resolved coverage of multiple lines would allow better rejection of spatial pixels influenced by AGNs or shock ionization based on the BPT diagram.

This analysis has highlighted the need for high-quality data with sufficient spatial resolution, S/N, and wavelength coverage to disentangle the physical processes driving the observed line ratios and to pin down the intrinsic abundance gradients. Our understanding of the global and resolved metallicity distributions among and within SFGs, as well as their cosmic evolution, will benefit greatly from the added resolution and sensitivity of *JWST* and the Extremely Large Telescopes.

We thank the referee for a thorough reading of the manuscript and helpful comments. M.F. and D.W. acknowledge the support of the Deutsche Forschungs Gemeinschaft (DFG) via Project WI 3871/1-1. J.C. acknowledges the support of the Deutsche Zentrum für Luft- und Raumfahrt (DLR) via Project ID 50OR1513.

APPENDIX

Table 3 provides an overview of target properties for all galaxies where the $[\text{N II}]/\text{H}\alpha$ ratio could be measured. Figure 11 shows the $\text{H}\alpha$, velocity and $[\text{N II}]/\text{H}\alpha$ map as well as the $[\text{N II}]/\text{H}\alpha$ ratio as a function of radius for five example galaxies to illustrate the measurement of metallicity gradients. Figure 12 visualizes how we derive the necessary beam smearing correction for three example galaxies.

Table 3
Target Properties

#	z	$\log(M_*/M_\odot)$	r_e (kpc)	SFR _{Hα} ^a ($M_\odot \text{ yr}^{-1}$)	[N II]/H α ^b	$\Delta N2/\Delta r$ ^c (dex kpc ⁻¹)	Beam ^d
1	0.758	10.66	6.4	5.5	0.41 ± 0.03	0.004 ± 0.016	1.3
2	0.775	10.94	4.1	0.9	<0.11
3	0.777	10.35	2.9	24.7	0.44 ± 0.03	-0.013 ± 0.015	3.4
4	0.787	10.78	2.3	4.6	0.56 ± 0.03	-0.038 ± 0.013	3.3
5	0.787	10.51	5.0	21.0	0.41 ± 0.03	-0.050 ± 0.014	2.1
6	0.798	10.68	2.3	36.8	0.44 ± 0.01	-0.018 ± 0.004	2.5
7	0.799	10.63	4.3	21.0	0.42 ± 0.02	0.003 ± 0.010	2.1
8	0.803	10.58	4.7	5.5	0.37 ± 0.02	-0.015 ± 0.009	1.4
9	0.803	10.57	1.7	3.8	0.48 ± 0.03	0.041 ± 0.015	2.6
10	0.803	10.48	2.4	2.2	0.41 ± 0.02	-0.007 ± 0.011	2.1
11	0.809	10.22	5.3	2.6	0.22 ± 0.02	-0.022 ± 0.016	1.7
12	0.813	10.64	2.5	0.8	<0.20
13	0.822	11.01	4.0	99.8	0.93 ± 0.02	0.011 ± 0.008	2.0
14	0.822	9.81	2.2	17.9	<0.24
15	0.824	10.72	2.8	1.3	0.71 ± 0.11	0.050 ± 0.071	1.5
16	0.827	10.58	7.0	23.8	0.30 ± 0.02	-0.018 ± 0.010	1.3
17	0.828	10.69	4.1	78.6	0.50 ± 0.03	-0.013 ± 0.024	2.7
18	0.831	10.38	5.1	36.3	0.28 ± 0.03	0.000 ± 0.014	2.5
19	0.832	10.07	6.9	30.8	0.20 ± 0.01	-0.043 ± 0.007	1.7
20	0.834	10.55	2.0	6.1	0.44 ± 0.04	-0.040 ± 0.036	3.3
21	0.837	10.52	2.3	2.1	0.34 ± 0.02	-0.059 ± 0.023	4.9
22	0.839	10.83	3.3	3.9	0.89 ± 0.10	-0.092 ± 0.048	2.3
23	0.852	10.83	6.8	15.4	0.34 ± 0.02	-0.015 ± 0.008	1.8
24	0.854	10.73	8.3	23.5	0.31 ± 0.02	-0.003 ± 0.009	3.9
25	0.868	10.31	3.8	36.8	0.32 ± 0.01	0.013 ± 0.022	1.8
26	0.878	11.17	5.4	3.2	0.55 ± 0.08	-0.128 ± 0.048	3.2
27	0.879	9.82	5.5	4.4	0.13 ± 0.01	-0.035 ± 0.020	3.3
28	0.879	10.70	2.7	10.6	0.65 ± 0.02	0.024 ± 0.013	3.6
29	0.883	10.26	3.3	17.7	0.27 ± 0.02	-0.006 ± 0.017	2.0
30	0.883	10.80	3.6	1.2	<0.40
31	0.890	10.72	6.0	10.5	0.60 ± 0.03	-0.041 ± 0.016	2.7
32	0.890	10.95	5.4	2.7	0.48 ± 0.05	-0.028 ± 0.025	1.8
33	0.890	9.84	4.8	3.2	0.37 ± 0.05	0.042 ± 0.024	2.9
34	0.892	10.16	2.9	16.9	0.34 ± 0.02	-0.000 ± 0.011	2.5
35	0.892	10.03	10.1	26.9	0.15 ± 0.02	-0.034 ± 0.045	2.6
36	0.892	9.82	5.0	13.3	0.21 ± 0.01	-0.015 ± 0.015	2.0
37	0.893	10.71	8.4	8.6	0.29 ± 0.03	-0.030 ± 0.011	2.4
38	0.893	10.55	2.0	10.2	0.42 ± 0.01	-0.010 ± 0.007	2.3
39	0.893	9.88	1.9	6.5	0.20 ± 0.01	-0.007 ± 0.014	4.3
40	0.893	10.17	7.7	6.4	0.29 ± 0.03	-0.007 ± 0.022	1.9
41	0.894	9.82	1.2	21.8	0.37 ± 0.02	-0.016 ± 0.011	3.5
42	0.895	10.17	3.9	1.4	<0.19
43	0.896	10.18	3.2	22.1	0.32 ± 0.01	0.003 ± 0.007	1.8
44	0.896	10.29	3.8	7.7	0.11 ± 0.01	-0.043 ± 0.013	1.8
45	0.897	10.52	4.5	9.3	0.34 ± 0.01	-0.003 ± 0.006	1.7
46	0.897	10.75	5.6	18.3	0.43 ± 0.01	-0.019 ± 0.005	1.8
47	0.899	9.63	2.2	1.3	<0.50
48	0.899	10.20	0.9	0.2	<0.33
49	0.900	10.30	2.9	60.7	0.50 ± 0.01	-0.005 ± 0.009	1.9
50	0.900	10.31	3.8	19.0	0.35 ± 0.01	0.000 ± 0.005	1.8
51	0.901	10.10	3.1	2.8	0.45 ± 0.04	0.014 ± 0.021	2.1
52	0.902	10.46	4.7	10.7	0.24 ± 0.01	0.002 ± 0.006	2.0
53	0.905	10.16	3.4	12.9	0.65 ± 0.08	0.076 ± 0.035	3.5
54	0.907	10.79	2.7	1.5	1.33 ± 0.11
55	0.907	10.85	4.1	14.1	0.44 ± 0.02	-0.008 ± 0.006	1.8
56	0.907	10.77	4.2	29.3	0.40 ± 0.01	0.011 ± 0.005	1.7
57	0.912	10.43	****	1.2	0.88 ± 0.21
58	0.912	10.02	2.4	12.0	0.13 ± 0.01	-0.032 ± 0.019	3.1
59	0.912	10.92	3.5	6.3	0.33 ± 0.04	-0.067 ± 0.044	2.7
60	0.912	10.08	2.1	1.7	0.28 ± 0.04
61	0.913	10.25	3.4	4.8	0.12 ± 0.02
62	0.914	9.94	2.4	0.7	0.33 ± 0.05
63	0.914	10.21	8.1	4.4	<0.22
64	0.920	10.62	2.2	1.1	0.59 ± 0.26
65	0.920	9.88	4.3	5.2	0.25 ± 0.02
66	0.921	10.61	1.5	1.5	0.41 ± 0.06
67	0.922	10.17	3.0	15.5	0.38 ± 0.05	-0.019 ± 0.036	2.1

Table 3
(Continued)

#	z	$\log(M_*/M_\odot)$	r_e (kpc)	$\text{SFR}_{\text{H}\alpha}^a$ ($M_\odot \text{ yr}^{-1}$)	$[\text{N II}]/\text{H}\alpha^b$	$\Delta N2/\Delta r^c$ (dex kpc $^{-1}$)	Beam d
68	0.922	11.11	5.7	2.6	0.58 ± 0.03	-0.030 ± 0.010	2.6
69	0.949	10.17	6.1	14.6	0.32 ± 0.02	-0.016 ± 0.014	1.5
70	0.950	10.74	5.9	56.2	0.30 ± 0.03	-0.031 ± 0.020	2.6
71	0.952	10.10	3.2	5.2	0.26 ± 0.02	0.004 ± 0.016	2.4
72	0.953	9.91	4.1	14.3	0.13 ± 0.02	-0.078 ± 0.023	6.2
73	0.953	9.85	5.6	2.7	0.18 ± 0.02	0.010 ± 0.026	1.9
74	0.954	10.95	16.0	7.8	0.40 ± 0.01	0.002 ± 0.008	1.3
75	0.955	11.13	7.0	5.7	0.47 ± 0.03	-0.000 ± 0.013	1.3
76	0.975	10.80	2.5	1.2	0.53 ± 0.14
77	0.979	11.23	4.7	5.0	0.90 ± 0.05	-0.045 ± 0.031	1.8
78	0.997	10.43	6.6	2.7	0.18 ± 0.02
79	1.002	10.83	3.8	54.8	0.36 ± 0.02
80	1.004	10.29	4.3	23.5	0.56 ± 0.06	-0.006 ± 0.021	2.5
81	1.014	10.96	7.8	4.9	0.35 ± 0.07
82	1.015	10.43	0.5	2.4	0.53 ± 0.07	-0.072 ± 0.043	5.3
83	1.016	10.18	3.9	13.6	0.13 ± 0.03
84	1.017	10.42	3.1	8.4	0.30 ± 0.04	-0.022 ± 0.060	3.8
85	1.018	10.52	4.0	0.7	<0.40
86	1.018	10.31	6.6	34.7	0.29 ± 0.01	-0.023 ± 0.006	1.4
87	1.019	10.51	7.8	5.4	<0.17
88	1.022	10.12	3.0	1.2	0.30 ± 0.05
89	1.024	10.61	2.6	3.9	0.53 ± 0.04	0.003 ± 0.033	2.5
90	1.029	10.07	3.3	21.3	0.31 ± 0.01	-0.005 ± 0.013	2.6
91	1.031	10.40	6.1	9.5	0.22 ± 0.02	0.082 ± 0.060	1.5
92	1.031	10.74	7.0	109.2	0.36 ± 0.01	-0.006 ± 0.002	1.5
93	1.031	11.12	3.9	1.3	1.06 ± 0.12
94	1.032	10.52	3.7	23.7	0.34 ± 0.03	-0.022 ± 0.024	1.9
95	1.032	10.80	6.5	37.1	0.30 ± 0.01	-0.020 ± 0.005	1.4
96	1.033	10.78	5.6	12.2	0.91 ± 0.08	0.022 ± 0.034	1.4
97	1.039	10.15	2.4	25.2	0.37 ± 0.01
98	1.306	10.70	6.1	20.3	0.45 ± 0.05	-0.060 ± 0.029	2.1
99	1.363	9.93	2.8	9.7	0.21 ± 0.02	-0.009 ± 0.018	2.6
100	1.365	11.21	2.1	78.8	0.84 ± 0.04	-0.036 ± 0.041	3.9
101	1.382	10.82	7.0	41.3	0.21 ± 0.03	-0.047 ± 0.034	2.2
102	1.418	10.72	3.7	21.5	0.21 ± 0.01	-0.027 ± 0.008	2.3
103	1.419	10.82	4.2	33.3	0.35 ± 0.04	-0.026 ± 0.031	2.3
104	1.427	10.01	3.2	6.2	0.25 ± 0.04	0.031 ± 0.044	2.1
105	1.427	10.26	2.1	21.0	0.23 ± 0.01	0.013 ± 0.006	2.5
106	1.463	9.76	2.8	10.5	0.19 ± 0.01	0.106 ± 0.013	2.3
107	1.497	10.34	9.7	34.0	0.32 ± 0.05	0.005 ± 0.022	2.3
108	1.498	10.31	3.0	23.1	0.28 ± 0.02	-0.036 ± 0.017	3.9
109	1.499	9.73	1.6	6.8	0.25 ± 0.03	0.027 ± 0.021	2.2
110	1.499	9.83	4.0	3.9	0.22 ± 0.04
111	1.503	10.27	3.1	14.4	0.25 ± 0.02	0.024 ± 0.015	2.0
112	1.510	10.99	4.7	13.7	0.76 ± 0.17	-0.032 ± 0.075	2.3
113	1.514	9.75	2.8	15.4	0.13 ± 0.03
114	1.514	10.05	2.0	43.0	0.19 ± 0.01	0.014 ± 0.009	2.9
115	1.517	10.25	1.4	41.4	0.26 ± 0.01	-0.014 ± 0.005	3.0
116	1.518	11.06	4.6	60.9	0.35 ± 0.02	-0.017 ± 0.008	1.9
117	1.525	9.81	2.9	12.0	0.12 ± 0.01	0.041 ± 0.037	1.8
118	1.525	10.40	1.9	60.7	0.37 ± 0.01	0.021 ± 0.009	1.8
119	1.525	10.92	7.6	11.0	0.50 ± 0.06	-0.020 ± 0.023	2.7
120	1.526	11.32	6.3	39.3	0.43 ± 0.04	-0.027 ± 0.009	1.5
121	1.548	10.80	2.8	67.3	0.36 ± 0.02	-0.015 ± 0.008	2.4
122	1.550	10.84	4.0	47.3	0.44 ± 0.04	0.030 ± 0.035	1.5
123	1.552	11.37	8.3	76.7	0.37 ± 0.03	-0.038 ± 0.013	1.7
124	1.588	10.63	3.3	62.6	0.38 ± 0.02	-0.015 ± 0.009	2.1
125	1.606	10.12	1.8	11.9	0.23 ± 0.05	0.043 ± 0.059	2.2
126	1.606	11.26	14.2	5.6	0.26 ± 0.05	-0.047 ± 0.037	1.3
127	1.610	10.49	3.1	6.1	0.19 ± 0.06
128	1.613	10.23	4.7	12.0	0.20 ± 0.01	-0.003 ± 0.020	1.5
129	1.614	10.61	5.0	32.4	0.25 ± 0.05	-0.032 ± 0.030	1.8
130	1.615	10.78	1.0	394.2	0.73 ± 0.01	0.009 ± 0.006	2.1
131	1.644	9.92	3.4	14.3	0.19 ± 0.03	0.072 ± 0.048	1.5
132	1.651	10.15	1.6	29.1	0.14 ± 0.01	-0.023 ± 0.009	3.4
133	1.655	10.09	2.9	23.7	0.17 ± 0.01	0.018 ± 0.011	2.8
134	1.656	10.04	3.5	11.5	0.12 ± 0.02

Table 3
(Continued)

#	z	$\log(M_*/M_\odot)$	r_e (kpc)	$\text{SFR}_{\text{H}\alpha}^a$ ($M_\odot \text{ yr}^{-1}$)	$[\text{N II}]/\text{H}\alpha^b$	$\Delta N2/\Delta r^c$ (dex kpc $^{-1}$)	Beam ^d
135	1.656	9.89	4.0	57.2	0.13 ± 0.01	0.028 ± 0.014	2.1
136	1.663	11.40	3.9	10.2	0.89 ± 0.09	-0.022 ± 0.046	2.4
137	1.665	10.77	6.6	19.4	0.31 ± 0.03	0.035 ± 0.012	2.7
138	1.996	9.79	1.2	52.8	0.17 ± 0.02
139	1.997	10.89	5.0	182.0	0.28 ± 0.01	0.057 ± 0.016	1.6
140	1.998	10.08	2.1	10.1	0.33 ± 0.00
141	2.001	9.93	2.7	25.8	<0.17
142	2.006	10.06	2.9	29.8	0.18 ± 0.02	0.015 ± 0.027	2.4
143	2.007	10.04	1.4	27.8	0.11 ± 0.03
144	2.008	10.20	2.8	43.8	0.17 ± 0.05
145	2.010	10.01	2.4	11.2	0.22 ± 0.04
146	2.019	10.82	2.7	138.5	0.45 ± 0.01	0.020 ± 0.008	2.1
147	2.028	10.29	4.0	28.9	0.15 ± 0.02	-0.020 ± 0.018	1.8
148	2.036	10.65	7.8	25.8	0.32 ± 0.04
149	2.036	10.28	1.4	17.9	<0.22
150	2.060	10.90	2.4	61.2	0.38 ± 0.04	0.002 ± 0.042	2.3
151	2.061	10.97	3.5	28.4	0.65 ± 0.10
152	2.063	10.75	4.2	81.8	0.25 ± 0.02	-0.019 ± 0.022	1.5
153	2.087	10.06	1.8	16.4	<0.14
154	2.091	10.45	4.2	66.9	0.13 ± 0.01	0.003 ± 0.021	1.5
155	2.095	11.28	2.5	61.7	0.90 ± 0.02
156	2.103	11.40	7.0	179.8	1.34 ± 0.10	-0.035 ± 0.025	1.8
157	2.122	9.79	7.3	362.1	0.41 ± 0.03	0.015 ± 0.021	2.2
158	2.127	10.12	3.0	29.2	0.19 ± 0.01
159	2.141	10.86	1.4	7.4	0.57 ± 0.04
160	2.151	10.06	3.4	25.0	0.12 ± 0.01	0.055 ± 0.031	1.8
161	2.152	10.54	3.1	27.7	0.33 ± 0.04	0.004 ± 0.027	2.0
162	2.156	10.43	3.3	46.1	0.17 ± 0.02	-0.011 ± 0.026	2.5
163	2.157	10.27	4.2	24.3	0.12 ± 0.02
164	2.161	10.23	1.2	29.4	0.22 ± 0.02	0.029 ± 0.021	2.2
165	2.163	10.35	3.5	42.7	0.20 ± 0.01	-0.017 ± 0.016	2.1
166	2.166	10.85	2.5	130.0	0.38 ± 0.01	-0.002 ± 0.021	2.0
167	2.167	10.67	4.1	132.2	0.26 ± 0.01	0.016 ± 0.011	1.6
168	2.167	10.23	3.8	15.6	<0.20
169	2.167	10.94	1.0	34.6	0.98 ± 0.21
170	2.171	10.03	2.5	29.0	<0.12
171	2.171	10.38	5.0	45.5	0.22 ± 0.02	0.026 ± 0.021	1.6
172	2.172	10.30	2.3	30.0	0.10 ± 0.01	-0.001 ± 0.015	3.2
173	2.173	10.15	6.5	15.6	0.18 ± 0.03	0.053 ± 0.056	1.5
174	2.177	10.06	1.4	24.9	0.16 ± 0.02
175	2.177	10.98	3.4	109.0	0.25 ± 0.02	-0.014 ± 0.024	2.1
176	2.179	11.01	3.0	104.8	0.38 ± 0.03	-0.006 ± 0.034	1.9
177	2.181	10.04	1.2	32.0	0.11 ± 0.01	0.014 ± 0.018	2.2
178	2.187	11.00	7.5	20.5	0.21 ± 0.04
179	2.189	10.68	2.7	43.5	0.21 ± 0.04
180	2.192	11.32	8.1	14.5	0.63 ± 0.10
181	2.193	10.79	7.5	61.7	0.22 ± 0.03
182	2.199	9.95	1.5	21.6	<0.11
183	2.215	10.37	3.9	20.3	0.32 ± 0.05
184	2.219	10.11	4.2	24.2	<0.10
185	2.222	10.26	2.4	13.6	0.17 ± 0.04
186	2.223	10.65	4.1	112.4	0.32 ± 0.04	0.027 ± 0.015	1.5
187	2.225	10.36	3.5	45.3	0.16 ± 0.03
188	2.227	10.50	2.4	58.1	0.46 ± 0.06	0.054 ± 0.031	2.1
189	2.227	10.36	4.3	35.9	0.22 ± 0.03
190	2.228	10.55	4.9	42.7	0.24 ± 0.04
191	2.229	10.61	2.5	112.6	0.24 ± 0.01	-0.026 ± 0.009	3.0
192	2.235	10.62	3.8	53.8	0.24 ± 0.02	0.002 ± 0.022	1.5
193	2.246	8.54	0.6	78.3	0.08 ± 0.02
194	2.248	11.09	2.4	4.1	<0.61
195	2.249	10.60	1.6	97.3	0.18 ± 0.01	-0.049 ± 0.027	3.5
196	2.254	10.65	3.4	108.4	0.29 ± 0.01	0.003 ± 0.012	1.8
197	2.257	10.12	2.6	24.2	0.18 ± 0.02	0.048 ± 0.020	2.1
198	2.290	11.28	2.5	397.8	0.45 ± 0.03	-0.031 ± 0.025	2.6
199	2.298	10.29	3.6	50.6	0.11 ± 0.02
200	2.298	10.27	2.7	23.5	0.22 ± 0.03	-0.041 ± 0.040	3.3
201	2.300	11.28	3.3	15.6	1.16 ± 0.18	0.090 ± 0.055	1.8

Table 3
(Continued)

#	z	$\log(M_*/M_\odot)$	r_e (kpc)	SFR _{Hα} ^a ($M_\odot \text{ yr}^{-1}$)	[N II]/H α ^b	$\Delta N2/\Delta r$ ^c (dex kpc ⁻¹)	Beam ^d
202	2.301	10.83	1.8	17.4	0.51 ± 0.05	-0.036 ± 0.030	3.6
203	2.301	10.23	1.9	11.1	0.23 ± 0.05
204	2.302	10.96	3.5	15.4	0.31 ± 0.04	0.024 ± 0.039	2.0
205	2.302	10.61	1.9	70.2	0.24 ± 0.04
206	2.306	10.28	1.8	22.6	<0.10
207	2.307	10.46	3.4	104.6	0.16 ± 0.03	-0.041 ± 0.027	2.8
208	2.307	10.59	4.9	74.4	0.20 ± 0.02	0.013 ± 0.018	1.5
209	2.308	10.57	4.1	72.0	0.15 ± 0.02	-0.069 ± 0.040	2.5
210	2.309	10.96	2.5	101.6	0.39 ± 0.08
211	2.313	10.52	1.9	132.3	0.22 ± 0.03	0.010 ± 0.026	2.4
212	2.314	10.38	1.7	24.5	<0.16
213	2.318	10.30	2.6	30.2	<0.08
214	2.318	10.60	4.4	34.1	<0.23
215	2.321	11.12	5.3	58.3	0.44 ± 0.13
216	2.329	10.69	5.6	59.4	0.11 ± 0.02
217	2.359	10.57	2.5	93.9	0.28 ± 0.04	-0.058 ± 0.042	3.6
218	2.380	10.99	6.2	55.6	0.43 ± 0.08
219	2.381	10.19	1.6	49.1	<0.15
220	2.391	10.54	2.9	23.6	0.38 ± 0.07	0.040 ± 0.049	1.8
221	2.393	10.32	1.8	37.0	0.14 ± 0.04
222	2.406	10.85	1.4	63.9	0.48 ± 0.04
223	2.408	10.69	4.3	71.0	0.30 ± 0.04	-0.101 ± 0.040	4.0
224	2.431	10.96	0.7	44.9	0.55 ± 0.05	0.006 ± 0.029	2.1
225	2.437	10.53	4.0	171.9	0.28 ± 0.03
226	2.438	10.56	3.0	40.7	0.31 ± 0.05	-0.022 ± 0.044	2.1
227	2.439	10.93	4.7	58.1	0.38 ± 0.06	-0.015 ± 0.053	1.9
228	2.441	10.52	5.3	72.1	0.31 ± 0.04
229	2.442	10.66	2.9	75.0	0.29 ± 0.04
230	2.444	11.22	1.4	3.7	1.06 ± 0.28
231	2.453	11.01	1.2	50.7	0.91 ± 0.08	-0.052 ± 0.037	3.1
232	2.454	9.88	4.5	40.4	<0.11
233	2.460	10.29	0.9	53.3	0.19 ± 0.03
234	2.464	10.46	5.1	48.5	<0.15
235	2.466	10.85	2.7	57.0	0.29 ± 0.06
236	2.467	10.90	4.1	68.2	0.42 ± 0.08
237	2.467	10.52	2.0	42.6	0.21 ± 0.05
238	2.468	11.11	1.2	53.0	0.59 ± 0.05	-0.045 ± 0.028	3.1
239	2.469	10.85	6.0	112.7	0.31 ± 0.03	0.047 ± 0.028	1.5
240	2.469	10.68	4.3	111.7	0.16 ± 0.02	0.044 ± 0.042	1.5
241	2.469	10.79	4.2	59.3	<0.18
242	2.478	10.17	2.9	24.7	<0.19
243	2.479	10.43	3.1	19.8	<0.45
244	2.485	11.01	9.4	83.5	0.55 ± 0.10	0.033 ± 0.050	1.3
245	2.513	11.12	3.2	271.5	0.51 ± 0.07
246	2.519	11.22	6.2	131.3	0.60 ± 0.06	-0.016 ± 0.033	1.3
247	2.524	10.22	5.4	25.7	0.39 ± 0.11
248	2.525	11.13	3.9	18.2	0.77 ± 0.17
249	2.526	10.40	3.6	44.2	<0.18
250	2.529	11.15	4.8	53.0	0.39 ± 0.06
251	2.530	11.01	1.0	3.8	<0.44
252	2.530	10.88	5.1	35.4	0.50 ± 0.06	-0.019 ± 0.041	1.5
253	2.537	10.58	3.7	22.0	<0.33
254	2.540	10.71	3.7	45.8	<0.27
255	2.553	10.62	6.0	72.0	<0.26
256	2.563	11.03	4.5	156.3	0.47 ± 0.05	0.041 ± 0.023	1.5
257	2.569	10.26	2.6	133.3	0.34 ± 0.05
258	2.575	10.00	3.9	57.3	<0.11
259	2.583	10.50	3.3	61.0	<0.19

Notes.^a H α -based SFR corrected for dust extinction using the SED-derived reddening and accounting for additional extinction of the nebular lines following Wuyts et al. (2013).^b Integrated [N II]/H α ratio.^c Observed gradient in [N II]/H α , excluding the nuclear region for AGN-flagged targets. Reported only when measurable.^d Multiplicative beam-smearing correction factor for the N2 gradient, derived from simple analytical models assuming a smooth linear intrinsic radial gradient.

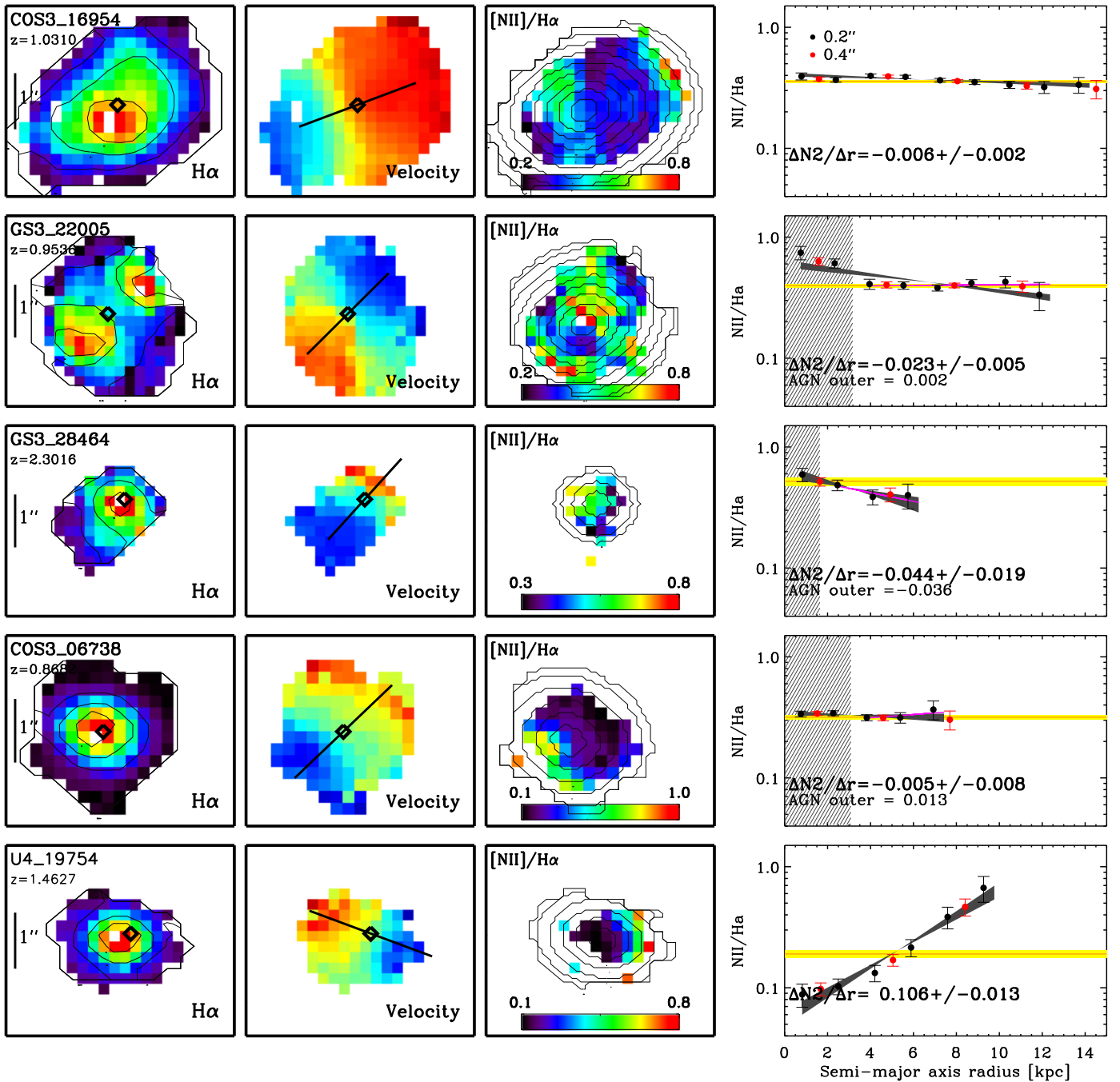


Figure 11. Illustration of how abundance gradients are measured for five example galaxies. The three panels on the left show the H α , velocity, and [N II]/H α maps, respectively, where in the last only pixels with S/N > 3 in [N II] are shown. In each panel, the black open diamond corresponds to the continuum center. The H α map additionally shows the H α contours, and the kinematic position angle is shown on the velocity map. Based on the center, PA, and ellipticity of the outer H α contours, we create 1 pixel wide elliptical apertures as shown on top of the [N II]/H α map in the third column. The chosen ellipticity does not significantly affect the measured gradient. The rightmost panels show the [N II]/H α ratios as a function of semimajor-axis radius for these apertures. The red data points correspond to the wider 2 pixel or 0.4'' apertures. The integrated [N II]/H α ratio and its uncertainty are indicated by the orange horizontal line and yellow band. The dark gray shaded band is the best-fit gradient and uncertainty. The middle three galaxies are each identified as an AGN. In this case we exclude the inner one or two apertures as indicated by the vertical gray shaded region, and we refit the remaining outer data points (magenta line). For the third and fourth galaxies, both fits are consistent. The second row shows an example where the [N II]/H α ratios in the center are significantly elevated due to the AGNs, such that the outer gradient is much flatter.

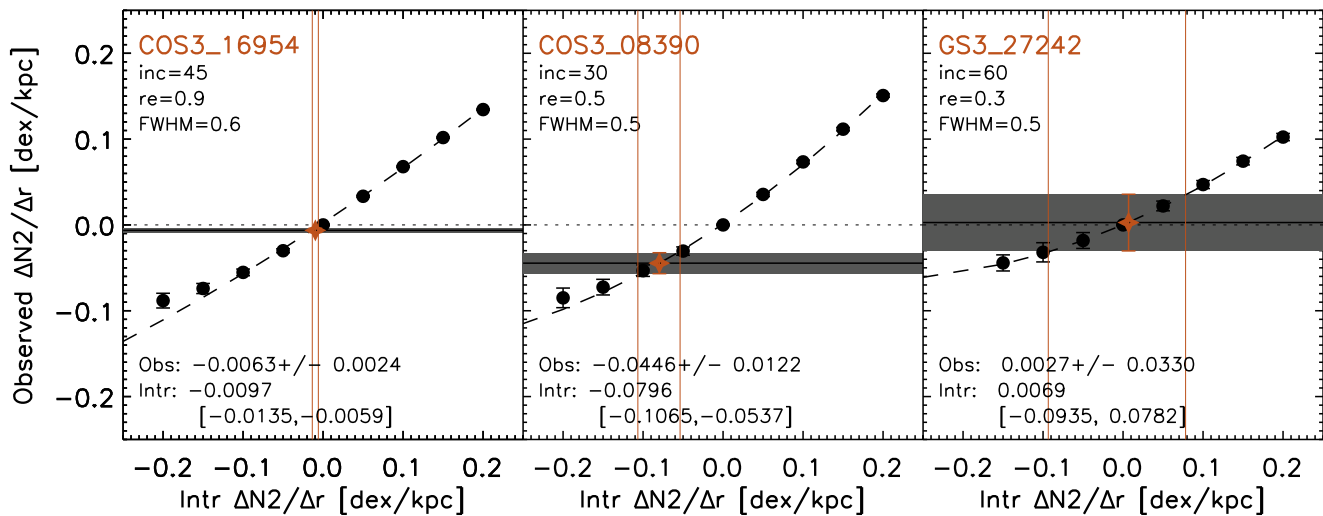


Figure 12. Three examples of the beam-smearing correction and intrinsic metallicity gradient. In each panel, the horizontal gray band and black line show the observed gradient and its uncertainty. The black circles correspond to the gradient we would have observed for a range of intrinsic gradients from -0.2 to 0.2 dex kpc^{-1} , given the known seeing, inclination, and effective radius of the target. We fit a polynomial to this correlation and invert it to derive the intrinsic gradient and uncertainties, which corresponds to the gradient we actually observed in the data. This is shown by the orange star and orange vertical lines. The observed and intrinsic gradients are noted in [dex kpc^{-1}] at the bottom of each panel. In the right panel, the relation between observed and intrinsic gradient is very flat due to the small effective radius and high inclination of the target, requiring a large correction. This additionally causes large uncertainties on the intrinsic gradient compared to the observed uncertainties.

REFERENCES

- Andrews, B. H., & Martini, P. 2013, *ApJ*, 765, 140
- Anglés-Alcázar, D., Davé, R., Özel, F., et al. 2014, *ApJ*, 782, 84
- Baldwin, J. A., Phillips, M. M., & Terlevich, R. 1981, *PASP*, 93, 5
- Belli, S., Jones, T., Ellis, R., et al. 2013, *ApJ*, 772, 141
- Blanc, G. A., Kewley, L. J., Vogt, F. P. A., et al. 2015, *ApJ*, 798, 99
- Bouché, N., Dekel, A., Genzel, R., et al. 2010, *ApJ*, 718, 1001
- Brammer, G. B., van Dokkum, P. G., Franx, M., et al. 2012, *ApJS*, 200, 13
- Bresolin, F., Kennicutt, R. C., & Ryan-Weber, E. 2012, *ApJ*, 750, 122
- Brooks, A. M., Governato, F., Booth, C. M., et al. 2007, *ApJL*, 655, L17
- Bruzual, G., & Charlot, S. 2003, *MNRAS*, 344, 1000
- Calzetti, D., Armus, L., Bohlin, R. C., et al. 2000, *ApJ*, 533, 682
- Chabrier, G. 2003, *PASP*, 115, 763
- Chiappini, C., Matteucci, F., & Romano, D. 2001, *ApJ*, 554, 1044
- Cid Fernandes, R., Stasińska, G., Mateus, A., & Vale Asari, N. 2011, *MNRAS*, 413, 1687
- Coil, A. L., Aird, J., Reddy, N., et al. 2015, *ApJ*, 801, 35
- Cresci, G., Hicks, E. K. S., Genzel, R., et al. 2009, *ApJ*, 697, 115
- Cresci, G., Mannucci, F., Maiolino, R., et al. 2010, *Natur*, 467, 811
- Cullen, F., Cirasuolo, M., McLure, R. J., et al. 2014, *MNRAS*, 440, 2300
- Dalcanton, J. J., Yoachim, P., & Bernstein, R. A. 2004, *ApJ*, 608, 189
- Davé, R., Finlator, K., & Oppenheimer, B. D. 2011, *MNRAS*, 416, 1354
- Davé, R., Finlator, K., & Oppenheimer, B. D. 2012, *MNRAS*, 421, 98
- Davies, R., Agudo Berbel, A., Wierorrek, E., et al. 2013, *A&A*, 558, A56
- Davies, R., Förster Schreiber, N. M., Cresci, G., et al. 2011, *ApJ*, 741, 69
- Dekel, A., & Burkert, A. 2014, *MNRAS*, 438, 1870
- Dekel, A., Sari, R., Ceverino, D., et al. 2009, *ApJ*, 703, 785
- Ellison, S. L., Patton, D. R., Simard, L., & McConnachie, A. W. 2008, *ApJL*, 672, L107
- Erb, D. K., Shapley, A. E., Pettini, M., et al. 2006, *ApJ*, 644, 813
- Few, C. G., Gibson, B. K., Courty, S., et al. 2012, *A&A*, 547, 63
- Finlator, K., & Davé, R. 2008, *MNRAS*, 385, 2181
- Förster Schreiber, N. M., Genzel, R., Bouché, N., et al. 2009, *ApJ*, 706, 1364
- Förster Schreiber, N. M., Genzel, R., Newman, S. F., et al. 2014, *ApJ*, 787, 38
- Fu, J., Hou, J. L., Yin, J., et al. 2009, *ApJ*, 696, 668
- Genel, S., Genzel, R., Bouché, N., et al. 2008, *ApJ*, 688, 789
- Genzel, R., Förster Schreiber, N. M., Rosario, D., et al. 2014, *ApJ*, 796, 7
- Genzel, R., Tacconi, L. J., Lutz, D., et al. 2015, *ApJ*, 800, 20
- Gibson, B. K., Pilkington, K., Brook, C. B., et al. 2013, *A&A*, 554, 47
- Goddard, Q. E., Bresolin, F., Kennicutt, R. C., et al. 2011, *MNRAS*, 412, 1246
- Grasshorn Gebhardt, H. S., Zeimann, G. R., Ciardullo, R., et al. 2015, arXiv:1511.08243
- Grogin, N. A., Kocevski, D. D., Faber, S. M., et al. 2011, *ApJS*, 197, 35
- Henry, A., Scarlata, C., Domínguez, A., et al. 2013, *ApJL*, 776, L27
- Ho, I.-T., Kudritzki, R.-P., Kewley, L. J., et al. 2015, *MNRAS*, 448, 2030
- Jones, T., Ellis, R. S., Jullo, E., et al. 2010, *AJ*, 725, L176
- Jones, T., Ellis, R. S., Richard, J., et al. 2013, *ApJ*, 765, 48
- Jones, T., Wang, X., Schmidt, K. B., et al. 2015, *AJ*, 149, 107
- Kewley, L. J., Dopita, M. A., Leitherer, C., et al. 2013, *ApJ*, 774, 100
- Kewley, L. J., Dopita, M. A., Sutherland, R. S., et al. 2001, *ApJ*, 556, 121
- Kewley, L. J., & Ellison, S. L. 2008, *ApJ*, 681, 1183
- Kewley, L. J., Rupke, D., Zahid, J. H., et al. 2010, *ApJ*, 721, 48
- Kobayashi, C., & Nakasato, N. 2011, *ApJ*, 729, 16
- Koekemoer, A. M., Faber, S. M., Ferguson, H. C., et al. 2011, *ApJS*, 197, 36
- Kriek, M., Shapley, A. E., Reddy, N. A., et al. 2015, *ApJS*, 218, 15
- Kriek, M., van Dokkum, P. G., Labbé, I., et al. 2009, *ApJ*, 700, 221
- Lackner, C. N., Silverman, J. D., Salvato, M., et al. 2014, *AJ*, 148, 137
- Leethochawalit, N., Jones, T. A., Ellis, R. S., et al. 2015, arXiv:1509.01279
- Lilly, S. J., Carollo, C. M., Pipino, A., Renzini, A., & Peng, Y. 2013, *ApJ*, 772, 119
- López-Sanjuan, C., Cenarro, A. J., Hernández-Monteagudo, C., et al. 2014, *A&A*, 564, A127
- Lotz, J. M., Davis, M., Faber, S. M., et al. 2008, *ApJ*, 672, 177
- Lu, Y., Blanc, G. A., & Benson, A. 2015, *ApJ*, 808, 129L
- Lutz, D., Poglitsch, A., Altieri, B., et al. 2011, *A&A*, 532, A90
- Magdis, G. E., Bureau, M., Stott, J. P., et al. 2016, *MNRAS*, 456, 4533
- Magnelli, B., Popesso, P., Berta, S., et al. 2013, *A&A*, 553, A132
- Maiolino, R., Nagao, T., Grazian, A., et al. 2008, *A&A*, 488, 463
- Man, A. W. S., Toft, S., Zirm, A. W., et al. 2012, *ApJ*, 744, 85
- Mannucci, F., Cresci, G., Maiolino, R., Marconi, A., & Gnerucci, A. 2010, *MNRAS*, 408, 2115
- Mollá, M., & Díaz, A. I. 2005, *MNRAS*, 358, 521
- Momcheva, I. G., Brammer, G. B., van Dokkum, P. G., et al. 2015, arXiv:1510.02106
- Newman, S. F., Buschkamp, P., Genzel, R., et al. 2014, *ApJ*, 781, 21
- Newman, S. F., Genzel, R., Förster-Schreiber, N. M., et al. 2012, *ApJ*, 761, 43
- Onodera, M., Carollo, C. M., Lilly, S., et al. 2016, arXiv:1602.02779
- Peebles, M. S., & Shankar, F. 2011, *MNRAS*, 417, 2962
- Perez, J., Michel-Dansac, L., & Tissera, P. B. 2011, *MNRAS*, 417, 580
- Pérez-Montero, E. 2014, *MNRAS*, 441, 2663
- Pettini, M., & Pagel, B. E. J. 2004, *MNRAS*, 348, L59
- Pilkington, K., Few, C. G., Gibson, B. K., et al. 2012, *A&A*, 540, 56
- Queyrel, J., Contini, T., Kissler-Patig, M., et al. 2012, *A&A*, 539, A93
- Rahimi, A., Kawata, D., Allende Prieto, C., et al. 2011, *MNRAS*, 415, 1469
- Rudie, G. C., Steidel, C. C., Trainor, R. F., et al. 2012, *ApJ*, 750, 67
- Rupke, D. S. N., Kewley, L. J., & Barnes, J. E. 2010a, *ApJ*, 710, 156L
- Rupke, D. S. N., Kewley, L. J., & Chien, L.-H. 2010b, *ApJ*, 723, 1255
- Salim, S., Lee, J. C., Davé, R., et al. 2015, *ApJ*, 808, 25

- Sánchez, S. F., Rosales-Ortega, F. F., Iglesias-Pramo, J., et al. 2014, *A&A*, **563**, 49
- Sanders, R. L., Shapley, A. E., Kriek, M., et al. 2015, *ApJ*, **799**, 138
- Shapley, A. E., Reddy, N. A., Kriek, M., et al. 2015, *ApJ*, **801**, 88
- Sharples, R., Bender, R., Agudo Berbel, A., et al. 2013, *Msngr*, **151**, 21
- Silverman, J. D., Kashino, D., Sanders, D., et al. 2015, *ApJS*, **220**, 12
- Skelton, R. E., Whitaker, K. E., & Momcheva, I. G. 2014, *ApJS*, **214**, 24
- Spitoni, E., Calura, F., Matteucci, F., et al. 2010, *A&A*, **514**, A73
- Stasińska, G., Cid Fernandes, R., Mateus, A., et al. 2006, *MNRAS*, **371**, 972
- Steidel, C. C., Rudie, G. C., Strom, A. L., et al. 2014, *ApJ*, **795**, 165
- Steidel, C. C., Shapley, A. E., Pettini, M., et al. 2004, *ApJ*, **604**, 534
- Storey, P. J., & Zeppen, C. J. 2000, *MNRAS*, **312**, 813
- Stott, J. P., Sobral, D., Bower, R., et al. 2013, *MNRAS*, **436**, 1130
- Stott, J. P., Sobral, D., Swinbank, A. M., et al. 2014, *MNRAS*, **443**, 2695
- Swinbank, A. M., Sobral, D., Smail, I., et al. 2012, *MNRAS*, **426**, 935
- Tacconi, L. J., Neri, R., Genzel, R., et al. 2013, *ApJ*, **768**, 74
- Torrey, P., Cox, T. J., Kewley, L., et al. 2012, *ApJ*, **746**, 108
- Tremonti, C. A., Heckman, T. M., Kauffmann, G., et al. 2004, *ApJ*, **613**, 898
- Troncoso, P., Maiolino, R., Sommariva, V., et al. 2014, *A&A*, **563**, 58
- van der Wel, A., Bell, E. F., Häussler, B., et al. 2012, *ApJS*, **203**, 24
- van Zee, L., Salzer, J. J., Haynes, M. P., et al. 1998, *AJ*, **116**, 2805
- Wisnioski, E., Förster Schreiber, N. M., Wuyts, S., et al. 2015, *ApJ*, **799**, 209
- Wuyts, E., Kurk, J., Förster Schreiber, N. M., et al. 2014, *ApJL*, **789**, L40
- Wuyts, S., Förster Schreiber, N. M., Lutz, D., et al. 2011, *ApJ*, **738**, 106
- Wuyts, S., Förster Schreiber, N. M., Nelson, E. J., et al. 2013, *ApJ*, **779**, 135
- Yuan, T.-T., Kewley, L. J., & Rich, J. 2013a, *ApJ*, **767**, 106
- Yuan, T.-T., Kewley, L. J., & Richard, J. 2013b, *ApJ*, **763**, 9
- Yuan, T.-T., Kewley, L. J., Swinbank, A. M., et al. 2011, *ApJL*, **732**, L14
- Zahid, H. J., Kashino, D., Silverman, J. D., et al. 2014, *ApJ*, **792**, 75
- Zahid, H. J., Kewley, L. J., & Bresolin, F. 2011, *ApJ*, **730**, 137
- Zaritsky, D., Kennicutt, R. C., Jr., & Huchra, J. P. 1994, *ApJ*, **420**, 87
- Zolotov, A., Dekel, A., Mandelker, N., et al. 2015, *MNRAS*, **450**, 2327